

β -Cyclodextrin-based geometrically frustrated amphiphiles as one-component, cell-specific and organ-specific nucleic acid delivery systems



Gonzalo Rivero-Barbarroja^a, José López-Fernández^b, Inmaculada Juárez-González^c, Carlos Fernández-Clavero^d, Christophe Di Giorgio^e, Itziar Vélaz^f, María J. Garrido^c, Juan M. Benito^b, Carmen Ortiz Mellet^{a,*}, Francisco Mendicuti^{d,*}, Conchita Tros de Ilarduya^{c,*}, José M. García Fernández^{b,*}

^a Department of Organic Chemistry, Faculty of Chemistry, University of Seville, 41012 Sevilla, Spain

^b Instituto de Investigaciones Químicas (IIQ), CSIC – Universidad de Sevilla, 41092 Sevilla, Spain

^c Department of Pharmaceutical Sciences, School of Pharmacy and Nutrition, University of Navarra, 31080 Pamplona, Spain

^d Departamento de Química Analítica, Química Física e Ingeniería Química and Instituto de Investigación Química "Andrés del Río", Universidad de Alcalá, Spain

^e Institut de Chimie Nice, UMR 7272, Université Côte d'Azur, F-06108 Nice, France

^f Department of Chemistry, School of Sciences, University of Navarra, 31080 Pamplona, Spain

ARTICLE INFO

Keywords:

Cyclodextrins
Non-viral gene delivery
Self-assembling
Molecular nanoparticles
Precision macromolecular synthesis

ABSTRACT

We introduce an innovative β -cyclodextrin (β CD)-prototype for delivering nucleic acids: “geometrically frustrated amphiphiles” (GFAs). GFAs are designed with cationic centers evenly distributed across the primary O6 and secondary O2 positions of the β CD scaffold, while hydrophobic tails are anchored at the seven O3 positions. Such distribution of functional elements differs from Janus-type architectures and enlarges the capacity for accessing strictly monodisperse variants. Changes at the molecular level can then be correlated with preferred self-assembly and plasmid DNA (pDNA) co-assembly behaviors. Specifically, GFAs undergo pH-dependent transition between bilayered to monolayered vesicles or individual molecules. GFA-pDNA nanocomplexes exhibit topological and internal order characteristics that are also a function of the GFA molecular architecture. Notably, adjusting the pK_a of the cationic heads and the hydrophilic-hydrophobic balance, pupa-like arrangements implying axial alignments of GFA units flanked by quasi-parallel pDNA segments are preferred. *In vitro* cell transfection studies revealed remarkable differences in relative performances, which corresponded to distinct organ targeting outcomes *in vivo*. This allowed for preferential delivery to the liver and lung, kidney or spleen. The results collectively highlight cyclodextrin-based GFAs as a promising class of molecular vectors capable of finely tuning cell and organ transfection selectivity.

1. Introduction

The introduction of nucleic acids into target cells offers a pathway for precise gene expression control, unlocking opportunities for personalized medicine and innovative therapeutic options (Dunbar et al., 2018). These prospects hinge critically on the efficient and safe delivery of nucleic acids to the intentional point of intervention (Sung & Kim, 2019). While viral vectors have demonstrated high efficiency and site specificity (Bulcha et al., 2021; Mancheño-Corvo & Martín-Duque,

2006) they pose risks such as severe immune responses, cellular toxicity, and genotoxicity (Kaiser, 2018; Othman et al., 2021). Non-viral vectors, emerging as promising alternatives, offer improved safety profiles, ease of manufacturing, and potential for large-scale production (Dong et al., 2024; Lostalé-Seijo & Montenegro, 2018; Mendes et al., 2022; Zu & Gao, 2021). Among them, four-component lipid nanoparticles (LNPs), incorporating ionizable lipids, phospholipids, cholesterol, and polyethylene glycol (PEG)-conjugated lipids, have garnered attention as leading systems for nucleic acid delivery (Cullis & Hope, 2017; Hou

* Corresponding authors.

E-mail addresses: mellet@us.es (C. Ortiz Mellet), francisco.mendicuti@uah.es (F. Mendicuti), ctros@unav.es (C. Tros de Ilarduya), jogarcia@iiq.csic.es (J.M. García Fernández).

et al., 2021; Kulkarni et al., 2019), notably contributing to the success of mRNA-based COVID-19 vaccines (Chung et al., 2020; Rana et al., 2023; Rueda-Fernández et al., 2022; Verbeke et al., 2021). Notwithstanding, optimization of LNPs for broader clinical translation is hampered by the unknown distribution of their four components within the nanoparticle structure. The segregation of the neutral ionizable lipid as an oil phase in the LNP core hinders cytosolic release and significantly contributes to their low transfection efficiency (1–2 %) (Kulkarni et al., 2018; Ramezanpour et al., 2019). Moreover, LNPs are prone to stability issues that undermine both their integrity and efficacy (Schoenmaker et al., 2021; Blenke et al., 2023). Additionally, the use of PEG as a stealth coating on LNPs introduces the “PEG dilemma”: while extending LNP circulation time in the bloodstream, it concurrently diminishes gene expression by up to four orders of magnitude, primarily by reducing intracellular trafficking and impeding cellular uptake and endosomal escape (Hatakeyama et al., 2011; Whitfield et al., 2021). Additionally, PEG raises concerns regarding immunogenicity and potential off-target effects (Bigini et al., 2021; de Vrieze, 2021), underscoring the pressing need for targeted approaches to enhance therapeutic selectivity (Dilliard & Siegwart, 2023).

Addressing the limitations of LNPs and advancing nucleic acid therapeutics requires exploring novel strategies, focusing on precision chemistry, molecular engineering, and innovative design principles (Mitchell et al., 2021). In this context, molecular nanoparticle (MNP)-based systems, characterized by persistent shape and volume (Jiménez Blanco et al., 2017; Yin et al., 2017), have emerged as a highly promising class of nonviral vectors (Xu & Zhang, 2018). MNPs, such as polyhedral oligomeric silsesquioxanes (POSS) (Wang et al., 2018), fullerenes (C_{60}) (Kazemzadeh & Mozafari, 2019; Wang et al., 2017) polyoxometalates (POM) (Bijelic et al., 2019), and folded proteins (Moreno-Gutierrez et al., 2023) possess tunable structures and particle-like characteristics. This category also includes macrocyclic oligomers with limited flexibility composed of aromatic ((e.g. calixarenes (Sansone et al., 2006; Bagnacani et al., 2013; Barrán-Berdón et al., 2015; Liu, Zhang, et al., 2021) or pillararenes (Xiao et al., 2019; Zyryanov et al., 2023)), heterocyclic ((e.g. cucurbit[n]uryls (Chernikova & Berdnikova, 2020; Yuan et al., 2020))), monosaccharide ((e.g. cyclodextrins (Haley et al., 2020; Kali et al., 2024; Rivero-Barbarroja et al., 2020; Sehgal et al., 2024) or cyclotrehalans (Carbajo-Gordillo et al., 2020; Carbajo-Gordillo et al., 2022; Jiménez Blanco et al., 2016; Manzanares et al., 2017))) or amino acid building blocks ((e.g. regioselectively addressable functionalized template cyclopeptides - RAFTs (Bartolami et al., 2015))). Importantly, the distinctive geometries of MNPs and their ability to undergo regioselective elaboration can be leveraged to achieve efficient nanocomplexation and protection of nucleic acids. This opens up possibilities for the development of sequence-defined multifunctional prototypes, which can be incorporated into one-component vector formulations. By eliminating the need for complex lipid mixtures, these systems provide greater control over the delivery process, facilitating optimization for specific applications (Rhan et al., 2024).

The pursuit of MNP candidates represents a constantly sought-after objective in the field of gene therapy. However, progress in this domain has been somewhat constrained, predominantly within the scope of macrocyclic MNPs (Gallego-Yerga et al., 2015; Geng et al., 2019). Among them, cyclodextrins (CDs), with their unique toroidal structure, anisotropic distribution of hydroxyl groups and tunable host-guest interactions serve as privileged scaffolds (Mousazadeh et al., 2022; Ooi et al., 2024; Taharabaru et al., 2024). The precise molecular accuracy regarding composition, spatial relationships, and functionality renders these macromolecules exceptional for exploring the interplay between diverse molecular parameters in the hierarchical assembly processes that culminate in the formation of CD-nucleic acid nanocomplexes (CDplexes) (Bienvenu et al., 2012; Díaz-Moscóso et al., 2009; Gallego-Yerga et al., 2014). Through precision chemistry, cyclodextrin-based amphiphiles can be also functionalized with ligands or targeting moieties, enabling selective interaction with specific cells or tissues,

thereby enhancing the therapeutic specificity (Aranda et al., 2013; Gooding et al., 2015; Guo et al., 2012; McMahon et al., 2012; Méndez-Ardoy et al., 2015; Sun et al., 2023; Symens et al., 2012). However, the search for diastereomeric purity in conjunction with the incorporation of biorecognition modules entails relatively costly synthetic efforts (Díaz-Moscóso et al., 2011).

An appealing alternative that presents opportunities for ligand-devoid targeted delivery of nucleic acids consists in controlling factors such as size, shape, internal order, and surface charge of the nano-complexes (Jia et al., 2024). Recent research underscores the tangled relationship between the primary structure of lipid components in LNPs (Cheng et al., 2020; Liu, Cheng, et al., 2021) or amphiphilic Janus dendrimers-mRNA dendriplexes (Zhang, Atochina-Vasserman, Maurya, Huang, et al., 2021; Zhang, Atochina-Vasserman, Maurya, Liu, et al., 2021; Zhang et al., 2022; Percec & Sahoo, 2024) and their fate within the body. Similarly, our previous findings revealed that subtle modifications in the architecture of trehalose-based vectors can lead to diverse assembly behaviors, resulting in distinct nanocomplex topologies and specific selectivities towards certain organs and cells (Carbajo-Gordillo et al., 2019; Carbajo-Gordillo et al., 2021; Ortega-Caballero et al., 2024). In the case of CDs, the neat face distinction allows for efficient synthesis of Janus-type vectors with separate cationic and lipophilic domains located either at the primary and secondary rim (Fig. 1A) (Ortiz Mellet et al., 2011), or vice versa (Fig. 1B) (Ortega-Caballero et al., 2008). Upon co-assembly with nucleic acids, spherical nanoparticles featuring onion-like multilamellar arrangements of CD bilayers and DNA chains are obtained (Fig. 1C) (Villari et al., 2013), which show a broad range of cell transfection capabilities *in vitro* and a preferential tropism to the liver *in vivo*. Alternative self-assembling patterns have been attained by breaking the symmetry of the macrocycle, achieved through dimerization (Gallego-Yerga et al., 2018) or the incorporation of aromatic “clips” at specific locations (Neva et al., 2020). While distinct cell and organ selectivities were successfully attained through these approaches, the associated synthetic challenges are significantly heightened.

Here we proposed a new β CD-based nucleic acid delivery platform that surmounts the former archetype in its capacity to encode topological information. These vectors display cationic centers homogeneously distributed at both the primary O6 and the secondary O2 positions. The hydrophobic tails are then anchored at the seven O3 positions (Fig. 1D). Such distribution of functional elements frustrates the two-face sharp segregation of cationic and lipophilic domains characteristic of Janus MNPs. In the scientific literature, the term “frustrated amphiphiles” has been coined to refer to amphiphilic molecules for which the divergent alignment of the hydrophilic head and the lipid tail is hindered due to unfavorable hydrogen-bonding (Rutkauskaitė et al., 2022) or electrostatic interactions (Köstereli & Severin, 2012). By analogy, we use here “geometrically frustrated amphiphiles” (GFAs) to refer to amphiphilic MNPs for which the typical opposite orientation of hydrophilic and lipophilic moieties is disfavored by architectural constraints.

The goal of this publication is to present the design, synthesis and supramolecular properties of β CD-based cationizable GFAs, using principles built upon insights gained from Janus MNPs. In aqueous environments, these GFAs exhibit self-assembly into bilayer vesicles, with their stability significantly influenced by pH variations within the physiological range. Additionally, they demonstrate co-assembly with plasmid DNA (pDNA), leading to the formation of CDplexes upon a simple mixing process, thereby functioning as one-component delivery systems. Screening experiments with a library of 12 GFAs provide evidence regarding the significance of the vector’s primary structure in determining the physical characteristics of the resulting nanocomplexes. This encompasses the cationic heads and the hydrophobic part. Computational simulations (molecular mechanics and molecular dynamics; MM and MD), dynamic and static light scattering (DLS and SLS, respectively), and transmission electron microscopy (TEM) were utilized to assess the preferred interaction modes and the ensuing arrangements. *In vitro* and *in vivo* transfection experiments demonstrate the proof of

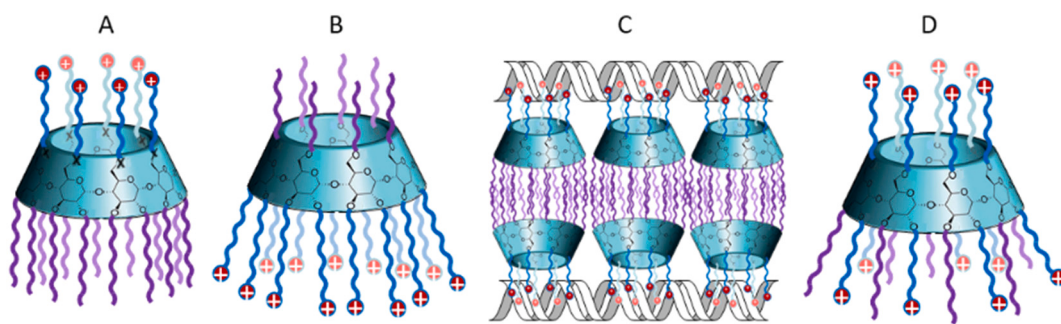


Fig. 1. A) and B) Schematic representation of Janus-type β CD-based cationizable amphiphiles showing the two possible relative dispositions of the cationic heads (red circles; X is generally oxygen or sulfur) and lipid tails (purple swinging lines). C) Typical lamellar arrangement in CDplexes co-assembled from Janus-type CD vectors and nucleic acids; the characteristic lipid bilayer organization of the amphiphilic CD component is shown. D) β CD-based geometrically frustrated amphiphiles proposed in this work.

concept of β CD-based ionizable GFAs, highlighting their potential utility as models to elucidate fundamental aspects of nonviral delivery systems across multiple scales and their potential applications in the formulation of cell- and organ-selective nucleic acid therapeutics.

2. Materials and methods

2.1. Materials

Ethylenediaminetetraacetic (EDTA) acid and DMSO Hibry-Max were supplied from Sigma. Sodium dodecyl sulfate (SDS) and NaCl (Roig Farma, Barcelona, Spain) were used to release DNA from the complexes. Alamar blue dye was purchased from Accumed International, Inc. (Westlake, OH, USA). The plasmid pCMV-Luc VR1216 (6934 bp) encoding luciferase was obtained from Clontech Laboratories, Inc. (Palo Alto, CA, USA). The plasmid pCMV100-IL-12 (5500 bp) encoding IL-12 was kindly provided by Dr. Chen Qian (University of Navarra, Spain). Cytokine levels were obtained using the kit BD OptEIA ELISA Set (BD Biosciences Pharmingen, San Diego, CA, USA) for IL-12 p40 following the manufacturer's instructions.

Heptakis(2,6-di-O-allyl-3-O-hexyl)cyclomaltoheptaose (**1**) was synthesized according to a previously reported procedure (Eskandani et al., 2011), with modifications to eliminate the need for column chromatography. Details of the synthesis are provided in the Supplementary data. The absence of mixtures of positional isomers was confirmed by the presence of a single spin system in the ^1H NMR spectrum (Fig. S62), consistent with the C_7 -molecular symmetry of the compound. Sample homogeneity was further supported by MS (Fig. S63) and combustion analysis, ruling out the presence of under- or over-allylated byproducts. Purity and homogeneity were systematically verified for all prepared batches of compound **1**.

2-(*tert*-Butoxycarbonylamino)ethyl isothiocyanate (**5**) (Benito et al., 2004), 2-(*N*-*tert*-butoxycarbonyl-*N*-methylamino)ethyl isothiocyanate (**6**) (Kim et al., 2015) and 2-[*N,N*-bis(2-(*tert*-butoxycarbonylamino)ethyl)amino]ethyl isothiocyanate (**7**) (Díaz-Moscoso et al., 2009) were prepared according to reported procedures. *N*-*tert*-butoxycarbonyl-2-aminoethanethiol (**4**) and 2-(4-morpholino)ethyl isothiocyanate (**8**) were purchased from BLD Pharmatech Ltd. (Reinbek, Germany). 2-(4-Hydroxypiperidino)ethyl isothiocyanate was prepared from 2-(4-aminopiperidino)ethylamine (BLD Pharmatech Ltd., Reinbek, Germany) by isothiocyanation reaction with thiophosgene as described in the Supplementary data.

Silica gel column chromatography was performed on silica gel 60 (E. Merck, 230–400 mesh) using 50 g of silica per 1 g of mixture. The crude product was loaded dissolved in the minimum amount of the less polar solvent component of the eluent. For Sephadex LH-20 size-exclusion chromatography purification, a ratio of 100 g of stationary phase per 1 g of crude material was used. The product was loaded dissolved in the

minimum amount of MeOH.

2.2. Synthesis

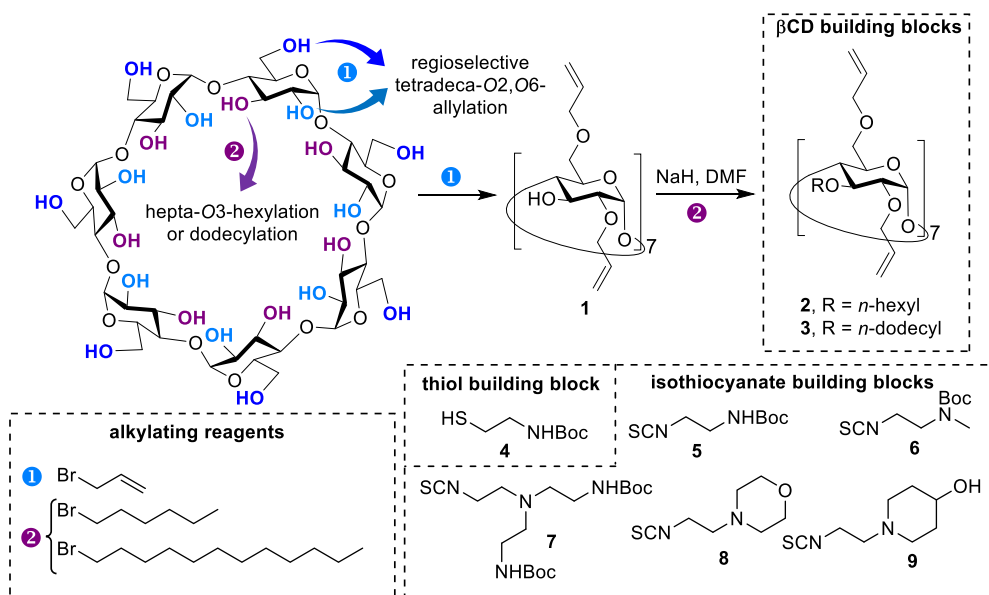
2.2.1. β CD-based GFA synthesis

As depicted in [Schemes 1 and 2](#), the synthesis of β -cyclodextrin-centered geometrically frustrated amphiphiles entailed: (a) per-(O3)-alkylation (hexylation or dodecylation) of the tetradecaallylated derivative **1** (\rightarrow **2** and **3**, respectively); (b) multiple thiol-ene coupling with Boc-protected cysteamine **4** (\rightarrow **10a,b**); (c) carbamate hydrolysis by treatment with aqueous TFA (\rightarrow **11a,b**); and (d) subsequent thiourea-forming reaction with either the Boc-protected aminoethyl isothiocyanates **5–7** (\rightarrow **12a,b–14a,b**), followed by a final deprotection step (\rightarrow **15a,b–17a,b**), or with the tertiary amine-equipped isothiocyanates **8** and **9** (\rightarrow **18a,b** and **19a,b**, respectively). Full characterization data are provided in the Supplementary data.

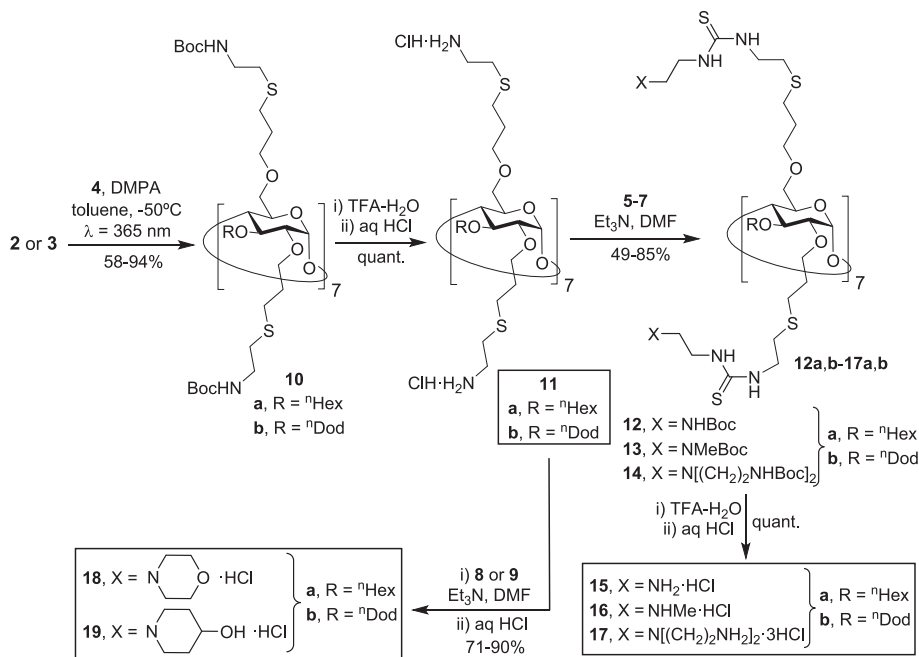
Heptakis(2,6-di-O-allyl-3-O-hexyl)cyclomaltoheptaose (**2**). To a chilled ($0\ ^\circ\text{C}$, ice-water bath) suspension of NaH (90 % purity, 220 mg, 8.26 mmol, 5 eq) in dry DMF (3 mL) under Ar atmosphere, a solution of heptakis(2,6-di-O-allyl)cyclomaltoheptaose **1** (400 mg, 0.236 mmol) in dry DMF (9 mL) was added. The ice-water bath was removed and the mixture was stirred for 1 h, allowing it to reach rt. 1-Bromohexane (1.16 mL, 8.26 mmol, 5 eq) was added, and stirring was continued for 16 h. The excess of NaH was quenched by dropwise addition of a small amount of MeOH, and the mixture was evaporated to dryness. A solution of the residue in DCM (10 mL) was washed with H_2O ($3 \times 5\ \text{mL}$) and brine ($1 \times 5\ \text{mL}$), dried (MgSO_4), evaporated and purified by column chromatography (1:10 \rightarrow 1:6 \rightarrow 1:2 EtOAc-cyclohexane). Yield 270 mg (50 %).

Heptakis(2,6-di-O-allyl-3-O-dodecyl)cyclomaltoheptaose (**3**). To a chilled ($0\ ^\circ\text{C}$, ice-water bath) suspension of NaH (90 % purity, 385 mg, 14.4 mmol, 5 eq) in dry DMF (5 mL) under Ar atmosphere, a solution of **1** (0.70 g, 0.413 mmol) in dry DMF (15 mL) was added. The ice-water bath was removed and the mixture was stirred for 1 h, allowing it to reach rt. 1-Bromododecane (3.5 mL, 14.4 mmol, 5 eq) was then added, and the mixture was heating at $60\ ^\circ\text{C}$ for 16 h. The excess of NaH was quenched by dropwise addition of a small amount of MeOH, and the mixture was evaporated to dryness. A solution of the residue in DCM (15 mL) was washed with H_2O ($3 \times 10\ \text{mL}$) and brine ($1 \times 10\ \text{mL}$), dried (MgSO_4), evaporated and purified by column chromatography (1:10 \rightarrow 1:2 EtOAc-cyclohexane). Yield: 1.08 g (91 %).

*Heptakis[2,6-di-O-(3-(2-(*N*-*tert*-butoxycarbonylamino)ethylthio)propyl]-3-O-hexyl]cyclomaltoheptaose* (**10a**). To a solution of **2** (270 mg, 0.118 mmol) and *N*-*tert*-butoxycarbonyl-2-aminoethanethiol **4** (558 μL , 3.31 mmol, 2 eq) in toluene (6 mL), 2,2-dimethoxy-2-phenylacetophenone (DMPA; 27 mg, 0.105 mmol) in toluene (0.5 mL) was added and the mixture was irradiated with UV light ($\lambda = 365\ \text{nm}$) at $-50\ ^\circ\text{C}$ under N_2 atmosphere for 1 h. The solvent was evaporated and the resulting



Scheme 1. Structures of the building blocks and reagents used in the synthesis of the β CD-based ionizable GFAs prepared in this work.



Scheme 2. Synthesis of β CD-scaffolded GFA library.

residue was purified by column chromatography (15:1 DCM-acetone \rightarrow 25:1 DCM-MeOH). Yield: 326 mg (58 %).

Heptakis[2,6-di-O-(3-(*N*-tert-butoxycarbonylamino)ethylthio)propyl]-3-O-dodecyl]cyclomaltoheptaose (10b**).** To a solution of **3** (500 mg, 0.174 mmol) and **4** (823 μL , 4.87 mmol, 2.0 eq) in toluene (3 mL), DMPA (50 mg, 0.194 mmol) in toluene (0.5 mL) was added and the mixture was irradiated with UV light ($\lambda = 365 \text{ nm}$) at -50°C under N_2 atmosphere for 1 h. The solvent was evaporated and the resulting residue was purified by column chromatography (50:1 \rightarrow 40:1 DCM-MeOH). Yield: 876 mg (94 %).

Heptakis[2,6-di-O-(3-(2-aminoethylthio)propyl)-3-O-hexyl]cyclomaltoheptaose tetradecahydrochloride (11a**).** Compound **10a** (0.49 g, 0.104 mmol) was dissolved in a 1:1 TFA-H₂O mixture (10 mL) and stirred at rt. for 1 h. The solvents were removed under reduced pressure

and the traces of TFA were coevaporated with toluene (4 \times 5 mL). The residue was dissolved in 0.1 M aqueous HCl and freeze-dried. Yield: 403 mg (quant).

Heptakis[2,6-di-O-(3-(2-aminoethylthio)propyl)-3-O-dodecyl]cyclomaltoheptaose tetrahydrochloride (11b**).** Compound **10b** (0.55 g, 0.103 mmol) was dissolved in a 1:1 TFA-H₂O mixture (10 mL) and stirred at rt. for 2 h. The solvents were removed under reduced pressure and the traces of TFA were coevaporated with toluene (4 \times 5 mL). The residue was dissolved in 0.1 M aqueous HCl and freeze-dried. Yield: 459 mg (quant).

Heptakis[2,6-di-O-(3-(2-(*N*-tert-butoxycarbonylamino)ethylthio)ethylthio)propyl]-3-O-hexyl]cyclomaltoheptaose (12a**).** To a solution of compound **11a** (115 mg, 29.7 μmol) in DMF (4 mL), Et₃N (75 μL , 0.54 mmol, 1.3 eq) and *2*-(*N*-tert-butoxycarbonylamino)ethyl-

isothiocyanate (**5**, 101 mg, 0.50 mmol, 1.2 eq) were sequentially added. The resulting clear solution was stirred overnight at room temperature without the formation of any precipitate. Afterward, the solvent was evaporated under reduced pressure. The remaining residue was then purified by Sephadex LH20 column using MeOH as eluent. Yield: 92 mg (50 %).

Heptakis[2,6-di-O-(3-(2-(2-N-tert-butoxycarbonylamino)ethylthioureido)ethylthio)propyl]-3-O-dodecyl]cyclomaltoheptaose (12b). To a solution of compound **11b** (101 mg, 22.4 µmol) in DMF (3.5 mL), Et₃N (56 µL, 0.407 mmol, 1.3 eq) and **5** (76 mg, 0.376 mmol, 1.2 eq) were sequentially added. The reaction mixture was stirred overnight at rt. and then the solvent was removed under reduced pressure. The resulting residue was purified by Sephadex LH20 column using MeOH as eluent. Yield: 129 mg (85 %).

Heptakis[2,6-di-O-(3-(2-(2-N-tert-butoxycarbonyl-N-methylamino)ethylthioureido)ethylthio)propyl]-3-O-hexyl]cyclomaltoheptaose (13a). To a solution of compound **11a** (205 mg, 52.9 µmol) in DMF (10 mL), Et₃N (205 µL, 1.48 mmol, 2 eq) and 2-(N-tert-butoxycarbonyl-N-methylamino)ethyl isothiocyanate (**6**, 319 mg, 1.48 mmol, 2 eq) were added sequentially. The resulting clear solution was stirred overnight at room temperature without the formation of any precipitate. Afterward, the solvent was evaporated under reduced pressure. The remaining residue was then purified by column chromatography (40:1 DCM-MeOH). Yield: 210 mg (62 %).

Heptakis[2,6-di-O-(3-(2-(2-N-tert-butoxycarbonyl-N-methylamino)ethylthioureido)ethylthio)propyl]-3-O-dodecyl]cyclomaltoheptaose (13b). To a solution of compound **11b** (69 mg, 15.4 µmol) in DMF (5 mL), Et₃N (37 µL, 0.27 mmol, 1.25 eq) and **6** (65 mg, 0.30 mmol, 1.4 eq) were added sequentially. The resulting clear solution was stirred overnight at room temperature without the formation of any precipitate. Afterward, the solvent was evaporated under reduced pressure. The remaining residue was then purified by column chromatography (25:1 DCM-MeOH). Yield: 79 mg (73 %).

Heptakis[2,6-di-O-(3-(2-(2-N,N-bis(2-N-tert-butoxycarbonylaminoethyl)amino)ethylthioureido)ethylthio)propyl]-3-O-hexyl]cyclomaltoheptaose (14a). To a solution of compound **11a** (80 mg, 20.6 µmol) in DMF (3.5 mL), Et₃N (52 µL, 0.376 mmol, 1.3 eq) and 2-[N,N-bis(2-(tert-butoxycarbonylamino)ethyl)amino]ethyl isothiocyanate (**7**, 135 mg, 0.347 mmol, 1.2 eq) were sequentially added. The reaction mixture was stirred overnight at rt. and then the solvent was removed under reduced pressure. The resulting residue was purified by Sephadex LH20 column using MeOH as eluent. Yield: 81.8 mg (45 %).

Heptakis[2,6-di-O-(3-(2-(2-N,N-bis(2-N-tert-butoxycarbonylaminoethyl)amino)ethylthioureido)ethylthio)propyl]-3-O-dodecyl]cyclomaltoheptaose (14b). To a solution of compound **11b** (112 mg, 25.1 µmol) in DMF (4 mL), Et₃N (63 µL, 0.45 mmol, 1.3 eq) and **7** (163 mg, 0.42 mmol, 1.2 eq) were sequentially added. The reaction mixture was stirred overnight at rt. and then the solvent was removed under reduced pressure. The resulting residue was purified by Sephadex LH20 column using MeOH as eluent. Yield: 162.6 mg (69 %).

Heptakis[2,6-di-O-(3-(2-(2-aminoethylthioureido)ethylthio)propyl)-3-O-hexyl]cyclomaltoheptaose tetrahydrochloride (15a). Compound **12a** (49.3 mg, 7.96 µmol) was dissolved in a 1:1 TFA-H₂O mixture (4 mL) and stirred at rt. for 1 h. The solvents were removed under reduced pressure and the traces of TFA were coevaporated with toluene (4 × 5 mL). The residue was dissolved in 0.1 M aqueous HCl and freeze-dried. Yield: 42 mg (quant).

Heptakis[2,6-di-O-(3-(2-(2-aminoethylthioureido)ethylthio)propyl)-3-O-dodecyl]cyclomaltoheptaose tetradecahydrochloride (15b). Compound **12b** (55 mg, 8.1 µmol) was dissolved in a 1:1 TFA-H₂O mixture (4 mL) and stirred at rt. for 2 h. The solvents were removed under reduced pressure and the traces of TFA were coevaporated with toluene (4 × 5 mL). The residue was dissolved 0.1 M aqueous HCl and freeze-dried. Yield: 48 mg (quant).

Heptakis[2,6-di-O-(3-(2-(2-N-methylamino)ethylthioureido)ethylthio)propyl]-3-O-hexyl]cyclomaltoheptaose tetradecahydrochloride (16a).

Compound **13a** (193 mg, 30.2 µmol) was dissolved in a 1:1 TFA-H₂O mixture (10 mL) and stirred at rt. for 2 h. The solvents were removed under reduced pressure and the traces of TFA were coevaporated with toluene (4 × 10 mL). The residue was dissolved in 0.1 M aqueous HCl and freeze-dried. Yield: 166 mg (quant).

Heptakis[2,6-di-O-(3-(2-(2-(N-methylamino)ethylthioureido)ethylthio)propyl)-3-O-dodecyl]cyclomaltoheptaose tetradecahydrochloride (16b). Compound **13b** (57 mg, 8.16 µmol) was dissolved in a 1:1 TFA-H₂O mixture (10 mL) and stirred at rt. for 1 h. The solvents were removed under reduced pressure and the traces of TFA were coevaporated with toluene (4 × 10 mL). The residue was dissolved in 0.1 M aqueous HCl and freeze-dried. Yield: 49 mg (quant).

Heptakis[2,6-di-O-(3-(2-(2-(N,N-bis(2-aminoethyl)amino)ethylthioureido)propyl)-3-O-hexyl]cyclomaltoheptaose (17a) dote-tracanthahydrochloride. Compound **14a** (60.6 mg, 6.9 µmol) was dissolved in a 1:1 TFA-H₂O mixture (3 mL) and stirred at rt. for 2 h. The solvents were removed under reduced pressure and the traces of TFA were coevaporated with toluene (4 × 5 mL). The residue was dissolved in 0.1 M aqueous HCl and freeze-dried. Yield: 48 mg (quant).

Heptakis[2,6-di-O-(3-(2-(2-(N,N-bis(2-aminoethyl)amino)ethylthioureido)propyl)-3-O-dodecyl]cyclomaltoheptaose (17b) dote-tracanthahydrochloride. Compound **14b** (60.2 mg, 6.4 µmol) was dissolved in a 1:1 TFA-H₂O mixture (4 mL) and stirred at rt. for 2 h. The solvents were removed under reduced pressure and the traces of TFA were coevaporated with toluene (4 × 5 mL). The residue was dissolved in 0.1 M aqueous HCl and freeze-dried. Yield: 49 mg (quant).

Heptakis[2,6-di-O-(3-(2-(2-(4-morpholino)ethylthioureido)ethylthio)propyl)-3-O-hexyl]cyclomaltoheptaose tetradecahydrochloride (18a). To a solution of compound **11a** (150 mg, 38.7 µmol) in DMF (5 mL), Et₃N (106 µL, 0.76 mmol, 1.4 eq) and 2-(4-morpholino)ethyl isothiocyanate (**8**, 115 mg, 0.66 mmol, 1.25 eq) were sequentially added. The reaction mixture was stirred overnight at rt. and then the solvent was removed at reduced pressure and the resulting residue was purified by Sephadex LH20 column using MeOH as eluent. The product-containing fraction was concentrated to dryness, dissolved in 0.1 M aqueous HCl and freeze-dried. Yield: 170 mg (71 %).

Heptakis[2,6-di-O-(3-(2-(2-(4-morpholino)ethylthioureido)ethylthio)propyl)-3-O-dodecyl]cyclomaltoheptaose tetradecahydrochloride (18b). To a solution of compound **11b** (138 mg, 30.9 µmol) in DMF (5 mL), Et₃N (78 µL, 0.56 mmol, 1.4 eq) and **8** (84 mg, 0.49 mmol, 1.25 eq) were sequentially added. The reaction mixture was stirred overnight at rt. and then the solvent was removed under reduced pressure. The resulting residue was purified by Sephadex LH20 column using MeOH as eluent. The product-containing fraction was concentrated to dryness, dissolved in 0.1 M aqueous HCl and freeze-dried. Yield: 167 mg (78 %).

Heptakis[2,6-di-O-(3-(2-(2-(4-hydroxypiperidino)ethylthioureido)ethylthio)propyl)-3-O-hexyl]cyclomaltoheptaose tetradecahydrochloride (19a). To a solution of compound **11a** (150 mg, 38.7 µmol) in 10:1 DMF-H₂O mixture (5.5 mL), Et₃N (106 µL, 0.76 mmol, 1.4 eq) and 1-(2-isothiocyanatoethyl)piperidin-4-ol **9** (124 mg, 0.66 mmol, 1.25 eq) were sequentially added. The reaction mixture was stirred overnight at rt. and then the solvents were removed under vacuum, the resulting residue was purified by Sephadex LH20 column using MeOH as eluent. The product-containing fraction was concentrated to dryness, dissolved in 0.1 M aqueous HCl and freeze-dried. Yield: 175 mg (71 %).

Heptakis[2,6-di-O-(3-(2-(2-(4-hydroxypiperidino)ethylthioureido)ethylthio)propyl)-3-O-dodecyl]cyclomaltoheptaose tetradecahydrochloride (19b). To a solution of compound **11b** (125 mg, 28 µmol) in 10:1 DMF-H₂O (5.5 mL), Et₃N (78 µL, 0.56 mmol, 1.4 eq) and **9** (89 mg, 0.48 mmol, 1.3 eq) were added consecutively and the reaction mixture was stirred overnight at rt. The solvents were then removed under reduced pressure and the resulting residue was purified by Sephadex LH20 column using MeOH as eluent. The product-containing fraction was concentrated to dryness, dissolved in 0.1 M aqueous HCl and freeze-dried. Yield: 180 mg (90 %).

2.3. Formulation of pDNA-GFA nanocomplexes

The stock solution of nucleic acid was prepared in ddH₂O at 1.0 mg/mL concentration. The stock solution of the GFA vector was prepared in 1:1 DMSO-ddH₂O at 5–10 mM concentration (depending on the cationic density), selected to achieve the desired N/P ratio of the final CDplexes upon formulation. Each CDplex formulation was prepared by mixing two purposely-prepared phases in 9:1 (v:v) ratio: (i) the nucleic acid phase in HEPES buffer (10 mM, pH 7.4) and (ii) the vector phase in 1:1 DMSO-ddH₂O. The nucleic acid phase was prepared from the stock solution by diluting 10-fold with HEPES, so that the final concentration was set up at 0.1 mg/mL ([phosphate] = 0.30 mM). The vector phase was prepared by diluting the corresponding vector stock with 1:1 DMSO-ddH₂O at the concentration required to achieve the desired N/P ratio, considering the number of cationizable groups in the vector molecular structure. Mixing was followed by gentle sample homogenization and storage at 4 °C until CDplexes were used. Particle size for each formulation was measured (DLS) immediately after preparation and monitored upon storage at 4 °C during several weeks without noticing relevant variations in size and polydispersity. Such formulation procedure ensures that the nucleic acid concentration, pH and DMSO ratio (5 % v:v) are identical throughout all formulations. For *in vitro* and *in vivo* assays, the formulations were diluted with HEPES buffer in order to reach a DMSO proportion below the 1 % threshold. Control experiments confirmed that the dilution process does not affect CDplex size and polydispersity.

As an illustrative example, the preparation of CDplexes from pDNA and **16b** at N/P 10 is detailed. Calculations were made for the preparation of 100 µL of the final pDNA-**16b** formulation, containing 0.1 mg/mL pDNA.

- Nucleic acid phase (100 µL)*. Prepared by diluting 11 µL of the 1.0 mg/mL ([phosphate] 3.0 mM) pDNA stock solution in the appropriate volume of HEPES buffer (10 mM, pH 7.4).
- Vector phase (100 µL)*. The concentration of the vector phase was calculated on the basis of the number of cationizable groups per molecule of the vector (14 in the case of **16b**), the desired N/P ratio (10 in the present example), and the 9:1 phase mixing ratio, according to the formula:

$$[\text{vector phase}] \times (n^{\circ} \text{ cationic groups})$$

$$= [\text{phosphate}]_{\text{formulation}} \times N / P_{\text{ratio}} \times (9 : 1 \text{ mixing ratio})$$

For an N/P 10 the required concentration of **16b** is 2.16 mM. It was achieved by diluting 43 µL of a 5 mM stock solution of **16b** with 1:1 DMSO-ddH₂O to a final 100 µL volume.

- Finally, the nucleic acid (90 µL) and vector (10 µL) phases were gently mixed and stored at 4 °C.

Detailed calculations for all formulations prepared in this work are collected in the Supplementary data, Tables S1 and S2.

The amount of GFA or control vector (bPEI) used in each formulation was calculated according to the desired pDNA concentration, the N/P ratio, the molecular weight, and the number of protonable nitrogen atoms in the corresponding cationic derivative. Typically, the plasmid pCMV-Luc VR1216 was diluted in HEPES (10 mM, pH 7.4) and then the required amount of GFA derivative or control vector was dispersed in this solution according the above from a stock solution in DMSO (typically 1–10 mM). The resulting mixture (with a final DMSO content below 1 % in all cases) was instantly vortexed thoroughly, and the complexes were incubated for 1 h at rt. prior to subjecting them to characterization or transfection experiments.

2.4. Procedure for determination of *in vitro* transfection activity

Cells (COS-7, HepG2, RAW264.7 or NPTr) were seeded in medium in 48-well plates (Iwaki Microplate, Japan) and incubated for 24 h at 37 °C in 5 % CO₂. The medium was removed, and 0.3 mL of complete medium (activated FBS) and 0.2 mL of CDplexes (containing 1 µg of pDNA) were added to each well. After 4 h incubation the medium was replaced for complete medium, and the cells were further incubated for 48 h. Cells were washed with phosphate-buffered saline (PBS) and lysed with 100 µL of Reporter Lysis Buffer (Promega, Madison, WI) at rt. for 10 min, followed by a freeze–thaw cycle. A 20 µL aliquot of the supernatant was assayed for total luciferase activity by using the luciferase assay reagent (Promega), according to the manufacturer's protocol. A luminometer (Sirius-2, Berthold Detection Systems, Innogenetics, Diagnóstica y Terapéutica, Barcelona, Spain) was used to measure luciferase activity. The protein content of the lysates was measured by de DC protein Assay Reagent (Bio-Rad, Hercules, CA) with bovine serum albumin as the standard. The data were expressed as picograms of luciferase (based on a standard curve for luciferase activity) per milligram of protein. Samples were analyzed in a plate spectrophotometer Power Wave XS and a data processor KC junior, BioTek.

2.5. Cell viability, Alamar blue assay

Cell viability was quantified by a modified AlamarBlue assay (Invitrogen). Briefly, 1 mL of 10 % (v/v) Alamar blue dye in complete medium was added to each well 24 h post-transfection. After 2.5 h of incubation at 37 °C, 200 µL of the supernatant was assayed by measuring the absorbance at 570 and 600 nm. Cell viability (as percentage of control cells) was calculated according to the formula $(A_{570} - A_{600}) / (A_{570} - A_{600})$ of treated cells $\times 100 / (A_{570} - A_{600})$ of control cells.

2.6. *In vivo* transfection activity

Balb-c mice (6–8 weeks of age, 20–25 g weight) were purchased from Harlan Ibérica Laboratories. All animals were studied in accordance with guidelines established by Directive 86/609/EEC and with the approval of the Committee on Animal Research at the University of Navarra-CIMA (id ES/31-2010-000132; accreditation number CEEA 017-19). Individual mice in groups of eight (four males and four females) were injected via the tail vein with 200 µL of CDplexes containing 50 µg of pCMV-Luc VR1216 plasmid DNA at N/P 5. Naked DNA was injected as control. Twenty-four hours after injection the mice were sacrificed. The liver, heart, kidneys, lungs, and spleen were collected and washed with cold PBS. We homogenized the organs with 1 mL of lysis buffer using a homogenizer at 5000 rpm (Mini-Beadbeater; BioSpec Products, Inc., Bartlesville, OK) and centrifuged at 10000 rpm for 3 min. A 20 µL aliquot of the supernatant was analyzed for luciferase activity following the same procedure as for *in vitro* assays. Cytokine levels were obtained using the kit BD OptEIA ELISA Set (Pharmingen, San Diego, CA, USA) for IL-12 p70 following the manufacturer's instructions. Values were calculated based on a standard curve. Samples were analyzed in a plate spectrophotometer Power Wave XS and a data processor KC junior, BioTek®.

2.7. Statistical analysis

Statistical analyses were performed using SPSS software from SPSS Inc. (Chicago, IL). The analysis of the transfection efficiency of CDplexes was performed with a two-tailed unpaired Student's *t*-test. *P* < 0.05 was considered statistically significant.

2.8. Molecular mechanics (MM) and molecular dynamics (MD) calculations

Molecular Mechanics (MM) and Molecular Dynamics (MD)

calculations were performed to study the stability of a fully protonated GFA dimer in the presence of two B-DNA helical fragments in explicit water. Compound **15b** was selected for this purpose. The Sybyl X-2.0 (SYBYL-X 2.0; Tripos Associates; St. Louis, MO, 2012) and the Tripos Force Field were used for all calculations (Clark et al., 1989). B-DNA fragments contained twelve nucleotides with a CGCGAATTCTCGCG sequence each. Charges for **15b** were obtained by MOPAC (AM1) using the Gaussian program (Frisch et al., 2009), to provide a total net charge of +14 (esu) in the absence of chloride ions. DNA fragment charges were obtained by using the Gasteiger and Marsili method (Gasteiger & Marsili, 1980; Gasteiger & Marsili, 1987). The Molecular Silverware algorithm (MS) and periodic boundary conditions (PBC) were used for solvation (Blanco, 1991). A relative permittivity $\epsilon = 1.0$ was used for electrostatic contributions in explicit water. Nonbonded cutoff distances were set at 12 Å. Optimizations were performed with the simplex algorithm, and the conjugate gradient was used as a termination method with gradients of 3.0 kcal/(mol Å) for the MM calculations (Brunel et al., 1975; Press et al., 2007).

Initially, a neutralized (uncharged) **15b** dimer formation and its stability in water was studied by MM. In the neutral structure, the N···Cl virtual bonds lengths located at the end of the hydrophilic chains were constrained to keep them near the length for the minimum of the potential energy. For this purpose, a harmonic penalty function equation for the length of the bonds between the N and Cl atoms was added to the force field. This energy function was written as $E = k(l - l_e)^2$, where $k = 200 \text{ kcal/mol}\text{\AA}^2$, and l_e and l are the most favorable N···Cl length and the variable distance during the MD trajectory, respectively. The optimized (gradient 0.5 kcal/mol Å) minima binding energy (MBE) structures for the neutral dimer structures were used as the initial conformations for the 1.0 ns MD simulations in the presence of water. During MD, the bonds where H atoms were involved were constrained from vibrating, but the rest of the conformational parameters were variable. Trajectories were performed starting from 1 K, and the temperature was increased by 20 K intervals equilibrating the system at each intermediate temperature for 500 fs up to reaching the temperature of interest of 300 K. Once at this temperature, an additional equilibration period of up to 25 ps was used. The whole heating/equilibration period was discarded from the analysis. From this point on, the rest of the trajectory time (ns) was simulated at 2 fs integration time steps. The velocities were rescaled at 10 fs intervals. Structures obtained from the analysis of MD trajectories were saved every 500 fs, yielding n snapshots [$n = \text{time (ns)} \times 10^6 / 500$] for subsequent analysis.

The $(\mathbf{15b})_2\text{-}(DNA)_2$ complex formation and stability in water was also studied by MM and MD. MM calculations for the most favorable **15b** dimer structure in the presence of two DNA helix fragments were performed. Two possible orientations of the dimer, relative to the DNA helix, were considered: (a) either the dimer was placed along the y -axis and perpendicular to the two DNA fragments or (b) parallel to them (along the z -axis. The proposed approach of the DNA fragments to the dimer was always through the major groove. Optimized MBE structures for the $(\mathbf{15b})_2\text{-}(DNA)_2$ (gradient 0.5 kcal/mol Å) were used as the starting conformations for MD simulations. To maintain a regular helical structure for the pair of DNA chains and to avoid the fraying of the end portions of the short DNA helix during MD, the simulations were performed on MBE structures where the N···HN hydrogen bond distances for each pair of DNA complementary bases were constrained to keep them constant. For this purpose, a harmonic penalty function was added to the force field for those atoms which were involved in the constraint. This energy function is written as $E = k(r - r_i)^2$, where $k = 200 \text{ kcal/mol}\text{\AA}^2$, and r_i and r are the initial distance and the variable distance during the MD trajectory, respectively. A full description of the computational methods and results is provided in the Supplementary data.

3. Results and discussion

3.1. GFA design criteria, synthesis and properties

Cyclodextrins exemplify how molecular architecture plays a defining role in the chemical reactivity of MNPs. Within the torus structure, the narrower and wider rims are flanked by primary and secondary hydroxyls, respectively. The narrower rim primary OH₆ hydroxyls exhibit higher nucleophilicity due to reduced steric hindrance. On the other hand, the OH₂ groups, owing to the intramolecular hydrogen bonding network, display increased acidity and can be readily deprotonated (pK_a of 12.2). Accessing the OH₃ position poses a relatively greater challenge. These fundamental principles provide a conceptual framework for achieving regioselective alkylation concurrently at positions O₂ and O₆. Allylation ($\rightarrow \mathbf{1}$) is particularly advantageous in this context (Eskandani et al., 2011). First, it enables modification of the remaining OH₃ hydroxyls for the incorporation of the lipid tails by a next alkylation reaction. We used hexyl ($\rightarrow \mathbf{2}$) and dodecyl bromide ($\rightarrow \mathbf{3}$) for this purpose. Second, the allyl groups in the compound keeping the free OH₃ groups or in the related hepta-(O₃)-hexyl and hepta-(O₃)-dodecyl ethers can be engaged in multiple thiol-ene “click” reaction (Sinha & Equbal, 2019) with *tert*-butoxycarbonyl (Boc)-protected cysteamine (**4**). The methodology implemented to generate molecular diversity at the cationic domain then relies upon design principles originally developed for the synthesis of polycationic amphiphilic Janus CDs, but refined and expedited. It involves the isothiocyanates **5–9** as crucial precursors (Scheme 1).

Photochemical addition of thiol **4** to the tetradeca-O-allyl βCD derivatives **2** and **3** proceeded smoothly at -50°C in toluene to give the corresponding thioethers **10a,b** in 58–94 % yield. Acid-promoted hydrolysis of the carbamate groups ($\rightarrow \mathbf{11a,b}$) then exposes 14 peripheral primary amino groups. Note that this step already unmasks the GFA feature in just four sequential reactions from commercial βCD. Each of the two pivotal tetradecacycteaminyl βCD thioethers **2** or **3** was coupled with five aminoethyl-type isothiocyanates (**5–9**). The reaction is highly efficient without need of catalyst and insensitive to moisture, meeting all the criteria of click chemistry (Barner-Kowollik et al., 2011). Potential oxidation of the amine reagent by molecular oxygen can be prevented by generating the free base *in situ* from the corresponding hydrochloride salt, avoiding prolonged storage. Moreover, the resulting thiourea segments provide anchoring centers for hydrogen bonding, which are known to interact with phosphate groups in biology and in synthetic supramolecular chemistry and have been previously found to promote reversible complexation of nucleic acids (Breton et al., 2011). Final hydrolysis of the Boc-protected primary or secondary amino groups in the respective adducts was monitored using ¹H and ¹³C NMR after converting the products into their respective perhydrochloride salts. The characteristic signals for the methyl ($\delta_{\text{H}} 1.5$, $\delta_{\text{C}} 29 \text{ ppm}$) and carbonyl groups ($\delta_{\text{C}} 157 \text{ ppm}$) of the *tert*-butoxycarbonyl residues completely disappeared, indicating successful transformation. In this manner, a set of twelve sequence-defined GFAs combining amino, *N*'-(2-aminoethyl) thioureido, *N*'-(2-(*N*-methylamino)ethyl)thioureido, *N*'-(2-(*N,N*-bis(2-aminoethyl)amino)ethyl)thioureido, *N*'-(2-(4-morpholin-1-yl)ethyl)thioureido or *N*'-(2-(4-hydroxypiperidin-1-yl)ethyl)thioureido moieties linked at positions O₂ and O₆ on the βCD platform through 3-thiopropyl segments and hexyl (**10a–15a**) or dodecyl tails attached at positions O₃ (**10b–15b**) was gathered (Scheme 2).

Assessing structural integrity through NMR was challenging due to significant line broadening caused by slow rotation around the N—C (=S) thiourea bonds (Jiménez Blanco et al., 1999). The substantial reduction in motion within the central core region of the GFA macromolecules also leads to an extended relaxation time for the associated carbon atoms, resulting in considerably lower intensities of their signals in the ¹³C NMR spectra compared to the carbon resonances of the external chains. It is important to note that such spectroscopic features do not indicate structural defects. Nonetheless, electrospray ionization

(ESI) mass spectrometry confirmed the expected molecular weights through pseudomolecular ions with exceptional molecular homogeneity considering the double click coupling synthetic strategy should quantitatively take place at 14 positions. Specifically, no pseudomolecular ions for *N*-dealkylation products were detected, which would be expected if *N*-oxidation of secondary or tertiary amino groups had occurred. Combustion analysis data were also compatible with sample homogeneity. Although these techniques cannot detect diastereomeric mixtures, the combined results strongly indicate a high level of purity in the target compounds.

3.2. Self-assembly of β CD-based GFAs

The spontaneous formation of self-assembled structures from amphiphilic (macro)molecules consisting of ionic and hydrophobic domains in aqueous environments intricately balances attractive and repulsive forces. Hydrophobic attraction, hydrogen bonding, and steric or electrostatic repulsion all play significant roles in this delicate equilibrium, often resulting in a diverse array of nanostructures that exhibit pH-responsive behavior. In our study, the cationizable groups on compounds **11a,b** and to **15a,b-19a,b** were strategically chosen to cover a range of pK_a values spanning approximately from 6 to 10. In principle, groups with pK_a values 5–7 will be predominantly neutral at pH around 7.4, the extracellular pH, while they will be mainly reprotonated at pH 4.5, the pH at the lysosome. This is expected to deeply impact the stability and the characteristics of their aggregates (Mixich et al., 2024). Conversely, cationizable groups with pK_a values over 8 will be essentially protonated at any physiological pH and thus less pH-sensitive in the biological environment. For compounds **11a** and **11b**, the pK_a value of the isolated cationizable heads may closely approach that of S-methyl cysteamine (**20**, pK_a 9.7). However, the intrinsic polarization of the thiourea segment in compounds **15a,b** to **19a,b** is predicted to decrease basicity compared to the corresponding alkylamine (García Fernández & Ortiz Mellet, 2000). To determine the intrinsic pK_a values, methylthiourea adducts, namely compounds **21–25**, were prepared and titrated. The corresponding data are presented in Fig. 2 (see the Supplementary data for experimental details). It must be emphasized, however, that any assumptions made regarding the intrinsic pK_a of the isolated heads should be approached cautiously when dealing with aggregates. The locally intense electrostatic potential at charged surfaces hinders the extent of protonation, typically resulting in an effective pK_a downshift of several pH units compared to the intrinsic pK_a and widen pH protonation-deprotonation range (Borisov et al., 2011).

To evaluate the pH sensitivity of the self-assembly properties of the compounds, we initially investigated the size and topology of their aggregates in pure water across a 0.2–500 μ M concentration range. This range corresponds to a pH change of approximately 2 units based on the intrinsic pK_a of the amine-type heads. The assessment involved a combination of dynamic and static light scattering (DLS and SLS), fluorescence spectroscopy measurements in the presence of a fixed concentration of pyrene (50 μ M), and transmission electron microscopy (TEM). DLS provides information on the hydrodynamic diameter (D_h) of

the aggregates, offering insights into rearrangements or dissociation into individual amphiphile molecules, whereas SLS provides the particle molecular weight (MW). On the other hand, the fluorescence excitation spectrum of pyrene experiences a significant shift when transitioning from bulk water to a hydrophobic environment. This phenomenon is commonly utilized to detect the formation of micelles with a hydrophobic core, thereby establishing the critical micellar concentration (CMC) of conventional amphiphiles (Hofmann et al., 2011). Notably, pyrene is also capable of entering the β CD cavity through the wider rim, forming an inclusion complex, making it a useful probe for judging the accessibility of β CD cavities within the aggregates (Udachin & Ripmeester, 1998). This dual role of pyrene enables the evaluation of surface properties and internal order of the aggregates.

DLS/SLS experiments revealed consistent patterns in the series of β CD-based GFAs **11b** and **15a,b** to **19a,b**. At the lower concentrations (higher pH values), objects with a diameter (D_h) of 37–65 nm were observed, which transformed into much smaller entities with a D_h of approximately 4 nm at higher concentrations (lower pH values). The estimated molecular weights (MW_{SLS}) of the latter matched those calculated from their molecular formula within the experimental error, indicating a dissociation process (Table 1). The fluorescence of pyrene from its excitation spectrum, with the emission fixed at λ_{ex} 372 nm, remained constant within the concentration range where only aggregates were present in the solution. Subsequently, it experienced a linear increase with concentration. The intersection point of these two linear regimes aligns with the concentration at which the disruption of the aggregates occurs according to DLS (transition concentration, C_t ; Supplementary data, Figs. S32-S43 and Table 1). This suggests that while individual β CD-based GFA molecules can form complexes with pyrene, the aggregates lack a hydrophobic interior capable of accommodating pyrene molecules. Additionally, the β CD cavity is inaccessible both within the internal core and at the external corona of the particles.

The determination of the pH of the solutions used in the previous experiments provided the corresponding transition pH (pH_t) value in each case, defined as the pH at which a shift between distinct mesophases occurs. Ensuing DLS/SLS experiments conducted at fixed GFA concentrations (5 and 50 μ M) and solution pH both below and above the pH_t values (pH 3 and 7, respectively), conclusively verified that the shift from vesicles to individual molecules is a pH-driven process independent of the concentration. The experimental data can be concealed assuming that at $pH > pH_t$ values only a fraction of the amine groups is protonated. This allows for intermolecular hydrophobic interactions between the lipophilic tails at the secondary face to be reinforced by additional hydrophobic contacts involving the linker moieties connecting the ionizable heads. Furthermore, hydrogen bonding interactions involving NH/C=S acceptor/donor thiourea groups may contribute to the stabilization of a bilayer vesicle architecture. As the pH decreases, coulombic repulsions exert a dominant influence, leading to the dissociation of the vesicles and enabling the formation of pyrene inclusion complexes. TEM micrographs recorded at concentrations above the respective pH_t confirmed the existence of the anticipated vesicles. Beyond the pH_t , the vesicles are no longer observable (Fig. 3).

The exception to the above scenario is the hexylated GFA **11a**, lacking the peripheral aminoethylthiourea segments. Whereas in the $pH > pH_t$ regime the behavior was comparable to the other GFAs, a transition to larger vesicular aggregates of approximately 150 nm occurred as the protonation degree gradually increased (Table 1 and Fig. 3). This restructuring concurred with a notable increase in pyrene fluorescence excitation spectrum within the solution, strongly suggesting that the broader rim of the β CD platform became exposed and accessible to pyrene molecules, aligning with a monolayer organization. It is important to note that the central region of the β CD-scaffolded GFA, which separates the two polycationic domains, consists primarily of hydrophobic thioalkyl spacers attached to both β CD faces. By rearranging into monolayer vesicles, the exposure of hydrophobic surfaces to bulk water is minimized, akin to classical bolaamphiphiles. In contrast, the

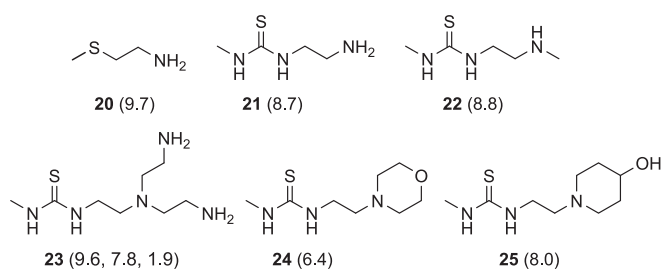


Fig. 2. Structure of the amines **20–25** used in titration experiments to assess the intrinsic pK_a values (in parenthesis) of the cationic heads displayed in the β CD GFAs prepared in this work.

Table 1

Transition concentration (C_t), transition pH (pH_t), average hydrodynamic diameter (D_h), polydispersity index (PDI), theoretical molecular weight (MW) and experimental molecular weight determined by SLS (MW_{SLS}) for aqueous solutions of compounds **11a,b** and **15a,b-19a,b**.

Comp.	C_t (μM)	pH_t	D_h above pH_t (nm)	PDI	D_h below pH_t (nm)	PDI	MW	MW _{SLS}
11a	6.0	3.4	53 ± 2	0.01	149 ± 18	0.16	3286.34	—
11b	4.5	3.6	54 ± 2	0.11	4.1 ± 0.3	0.19	4366.42	4485 ± 120
15a	5.1	3.9	52 ± 4	0.05	3.3 ± 0.4	0.23	5305.64	5384 ± 114
15b	10.1	3.8	64 ± 5	0.28	3.5 ± 0.3	0.16	5894.78	5906 ± 65
16a	4.2	4.7	37 ± 3	0.13	3.8 ± 0.4	0.2	5502.02	5617 ± 115
16b	28.2	4.5	45 ± 4	0.1	4.2 ± 0.4	0.14	6091.16	6135 ± 83
17a	44.4	3.4	65 ± 6	0.21	4.0 ± 0.3	0.06	7021.99	7120 ± 115
17b	54.1	3.1	43 ± 5	0.28	4.9 ± 0.4	0.15	7611.12	7802 ± 195
18a	11.7	3.6	55 ± 3	0.09	3.5 ± 0.3	0.18	6286.92	6318 ± 76
18b	46.1	3.4	62 ± 4	0.23	4.9 ± 0.3	0.13	6876.05	7003 ± 158
19a	18.7	4.7	40 ± 2	0.19	3.4 ± 0.2	0.1	6483.30	6512 ± 47
19b	4.8	5.0	63 ± 4	0.22	3.3 ± 0.3	0.12	7072.43	7201 ± 130

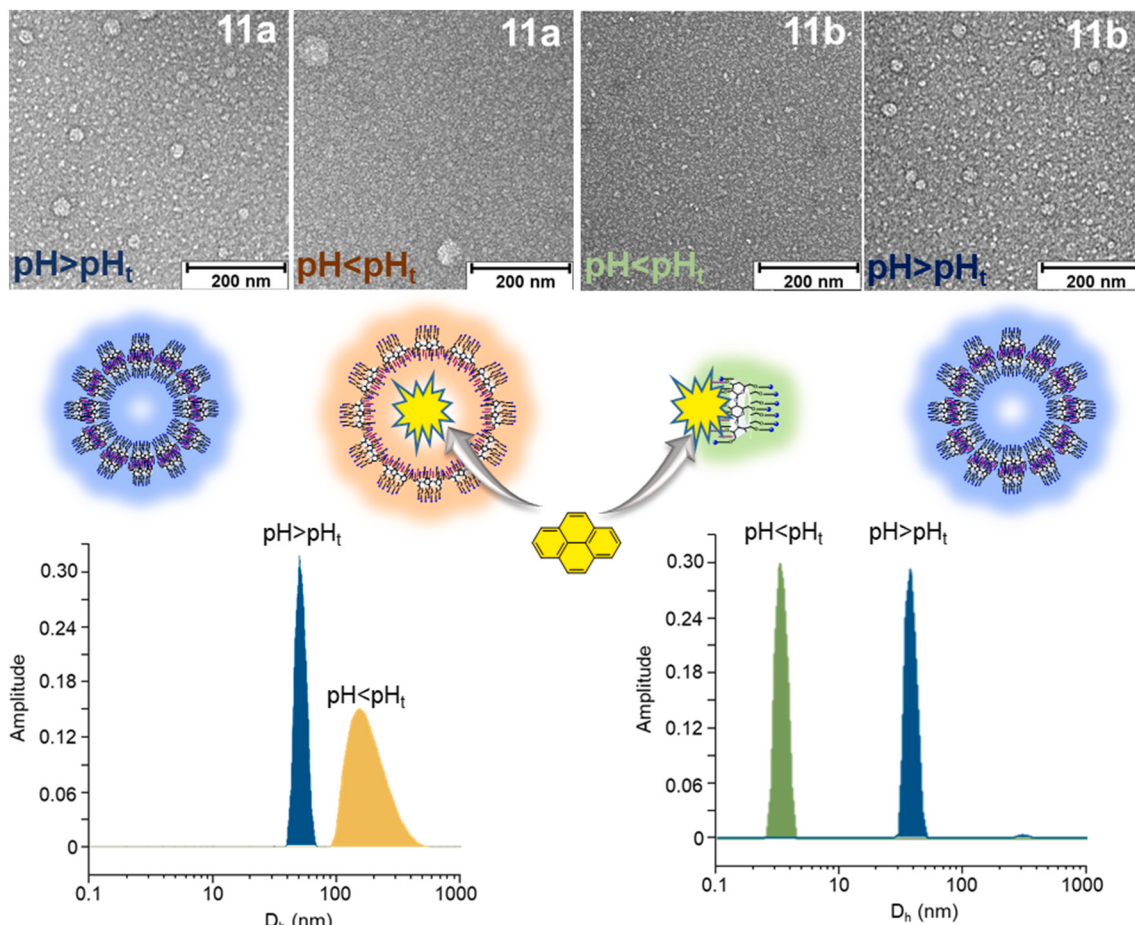


Fig. 3. Upper panel: Representative TEM micrographs recorded from aqueous solutions of **11a** and **11b** at pH above and below the pH_t. Middle panel: cartoons of the corresponding bilayer vesicles (blue), monolayer vesicles (orange) or individual molecules (green); the accessibility of the βCD secondary rim to pyrene inclusion in the two later cases, resulting in enhanced fluorescence emission, is indicated. Lower panel: DLS profiles recorded from the same aqueous solutions of **11a** and **11b**.

dodecylated counterpart **11b** would presumably expose the O3-linked longer lipid tails to the aqueous solvent, a thermodynamically unfavorable outcome. The higher hydrophilicity of protonated aminoethylthiourea segments further promotes dissociation *versus* monolayer vesicles in the case of **15a,b-19a,b**. This collective information provides a logical explanation for the experimental observations.

The cumulative findings support the prevalence of GFA bilayer configurations under the nearly neutral conditions applied in CDplex formulation. This dominance is expected to bolster the nucleic acid nanocondensation process by actively fostering desolvation through

hydrophobic effects, subsequent to the initial electrostatic interactions. Transitioning to monolayer arrangements (**11a**) or single molecules (**11b** and **15a,b-19a,b**) typically occurred within the pH range of 3.1 to 5.0 in the specified experimental conditions. In the context of GFA-nucleic acid co-assemblies, we anticipate that this shift would manifest at higher pH values, taking into account the influence of the anionization state of the polyphosphate chain on bilayer stability, suggesting the potential for distinct intralysosomal behaviors.

3.3. Co-assembly of GFAs with pDNA and GFA-pDNA nanocomplex characterization

The ability of the β CD derivatives **11a–11b** and **15a,b–19a,b** to form stable supramolecular CDplexes with pDNA (luciferase-encoding pCMV-LucVR1216) was determined at protonable nitrogen/phosphorus (N/P) ratios of 5 and 10 in 4-(2-hydroxyethyl)-1-piperazineethanesulfonic acid (HEPES) buffer (pH 7.4, 1 mM). DLS (Table 2) evidenced the formation of self-assembled nanoparticles, with positive ζ -potentials in the range 6–28 mV. Notably, the morpholine derivatives **18a** and **18b** stood out by affording CDplexes with negative surface charge for both formulations, aligning with the significantly lower intrinsic pK_a of this cationic head (24; Fig. 2). The average particle hydrodynamic diameter (D_h) systematically decreases on going from N/P 5 (115–253 nm) to N/P 10 (96–232 nm). Derivatives **15a,b–19a,b**, incorporating the thiourea segment, showed significantly smaller D_h values than the thiourea-devoid counterparts **11a,b** (Table 2). This highlights the influential role of hydrogen bonding interactions in nucleic acid nanocomplexation. Concerning the cationic centers, a trend of decreasing D_h values is observed as one moves from GFAs with only primary amino groups (**15a,b**) to those with secondary (**16a,b**), primary/tertiary (**17a,b**), or exclusively tertiary amino groups (**19a,b**). In contrast, no clear correlation was identified when comparing the effects of hexyl *versus* dodecyl lipid tails.

Formulations at N/P 5 were also examined using transmission electron microscopy (TEM) to gain insights into the shape and internal order of the CDplexes. The collective data demonstrates a clear correlation between the substitution pattern of the β CD scaffold and the vector/pDNA co-assembly behaviors. A comparative analysis of the TEM micrographs obtained from **11a,b** and **15a,b**, which differ in the presence or absence of thiourea groups in the ionizable domains and in the six- or twelve-carbon length of the lipid tails, illustrates this concept (Fig. 4). In terms of the O3-hexyl derivatives, **11a**/pDNA co-assemblies adopt a twisted thread-like structure, likely due to electrostatic interactions between the vector and the cargo that fail to facilitate efficient desolvation and protection of the plasmid. Consequently, these formulations were judged inappropriate for transfection purposes and were discarded for further studies. Conversely, **15a** forms rod-like CDplexes of approximately 150 nm. Moving to the O3-dodecyl representatives, in the case of **11b** the CDplexes take on a worm-like shape with somewhat irregular characteristics, while in the case of **15b** ellipsoidal topologies predominate. Indeed, all aminothiourea-equipped GFA-pDNA CDplexes formulated with **15a,b** to **19a,b** appeared as solid spheres or ellipsoids in TEM. However, the key differences laid in their internal structure. For the primary or secondary amine-terminated derivatives **15a,b** to **17a,b**, the dark domains inside the CDplexes predominantly formed and intricate interlocking of arcs, lacking a long-range order. In contrast, ordered

lamellar regions were more prominent in the case of **18a** and **19a**, which combined O3-hexyl tails with tertiary heterocyclic amines. Lastly, the O3-dodecyl compounds **18b** and **19b** predominantly formed CDplexes with pupa-like internal structures, characterized by alternating quasi-parallel arrangements of dark and light regions likely corresponding to plasmid chains and GFA alignments, respectively (Fig. 4).

DNA complex formation, protection, and overall DNA integrity in **11b** and **15a,b–19a,b** formulations was next assessed through electrophoresis mobility shift assay (EMSA) on a 0.8 % agarose gel, stained with the intercalating agent ethidium bromide. With the exception of **18a** and **18b** (already furnishing negatively-charged nanoparticles, Table 2), successful pDNA complexation and protection were evident. This was deduced from the compounds ability to halt the migration of pDNA within the gel, coupled with the recovery of essentially unaltered pDNA post-treatment with DNase I and sodium dodecyl sulfate (SDS) (Fig. 5).

3.4. Molecular mechanics and molecular dynamics simulations of GFA/pDNA co-assembly

Pupa-like patterns, either with spherical or ellipsoidal shape, have been previously documented in colloidal polymer nanoparticles (Ding et al., 2020; Ma et al., 2015) and, very recently, also in giant cationic amphiphile/anionic polyoxometalate co-assemblies (Wang et al., 2023). The transition from disorder to pupa-like constructions is influenced by various factors, such as the hydrophobic-hydrophilic balance in the amphiphile component and the interplay between the desolvation tendencies of the cationic and anionic partners. Disorder microphases arise from interactions involving discrete molecules, whereas lamellar microphases involve amphiphile-amphiphile interactions propagating in space, typically forming bilayers. Notwithstanding, the dark line-to-line distances within the pupa-like regions observed in GFA/pDNA CDplexes, approximately 3.5 nm as deduced from TEM micrographs, closely align with the diameter of a single GFA molecule in a computer-generated 3D model. This observation raises intriguing questions regarding the supramolecular interactions that govern the formation process of both disordered and layered nanoparticles in these systems.

To gain deeper understanding into the aforementioned conundrum, the GFA/pDNA co-assembly was investigated using molecular mechanics (MM) and molecular dynamics (MD) simulations. Compound **15b** was chosen as a prototypic representative for those studies. We anticipated that the presence of the longer dodecyl chains in **15b**, as compared with the hexyl chains in **15a**, would facilitate the identification of hydrophobic interaction-driven self- and co-assembly patterns *in silico*. Here, we provide a brief overview of the methodology, while detailed procedures can be found in the Supplementary data. Initially, a neutral **15b** dimer, with its ammonium groups neutralized by chloride anions, was generated and optimized (MM). In this calculation a molecule of **15b**, where charges from NH_3^+ terminal groups were neutralized by chloride atoms, was located with its center of mass (relative to the glycosidic oxygen atoms) at the origin of a coordinate system and oriented along the y -axis. Next, another neutral **15b** was approached along this axis. Fig. 6A depicts the procedure for the most favorable orientation, which involves facing the β CD secondary rims. The resulting minimum binding energy (MBE) structure represents the basic building block of a bilayer (Fig. 6B). Subsequently, the dimer was subjected to MD simulations in explicit water, demonstrating stability throughout the simulation period.

Next, the chloride counterions were removed from the MBE **15b**-dimer structure, and it was placed between two parallel DNA fragments, with phosphate groups anionized. Two different relative orientations were considered, namely the CD axis of symmetry of **15b**-dimer oriented perpendicularly (along the y -axis) or parallelly (along the z -axis) to the DNA helix axis (Fig. 7A), and analogous MM simulations were conducted. In both cases, the total interaction energy is negative, and monotonically decreased as the average of distances decreased, following the same trend of the electrostatics **15b**-dimer–DNA

Table 2

Average hydrodynamic diameter (D_h), polydispersity index (PDI) and ζ -potential values for N/P 5 and 10 formulations of GFAs **11a,b** and **15a,b–19a,b** with pDNA (luciferase-encoding pCMV-LucVR1216).

Comp.	N/P 5			N/P 10		
	D_h (nm)	PDI	ζ (mV)	D_h (nm)	PDI	ζ (mV)
11a	253 ± 49	0.264	18.0	232 ± 37	0.252	19.3
11b	199 ± 32	0.283	22.3	182 ± 20	0.175	25.4
15a	184 ± 17	0.255	15.6	158 ± 22	0.269	16.1
15b	195 ± 35	0.306	9.2	162 ± 18	0.276	17.8
16a	151 ± 13	0.123	15.4	134 ± 15	0.152	8.6
16b	177 ± 29	0.189	22.1	146 ± 21	0.244	25.8
17a	142 ± 11	0.156	6.2	129 ± 8	0.238	20.6
17b	132 ± 9	0.204	13.0	96 ± 8	0.192	14.1
18a	159 ± 23	0.251	-25.6	105 ± 12	0.234	-30.8
18b	115 ± 10	0.245	-26.4	111 ± 10	0.234	-25.8
19a	122 ± 12	0.215	16.6	98 ± 6	0.225	26.3
19b	130 ± 14	0.275	18.9	117 ± 9	0.250	20.8

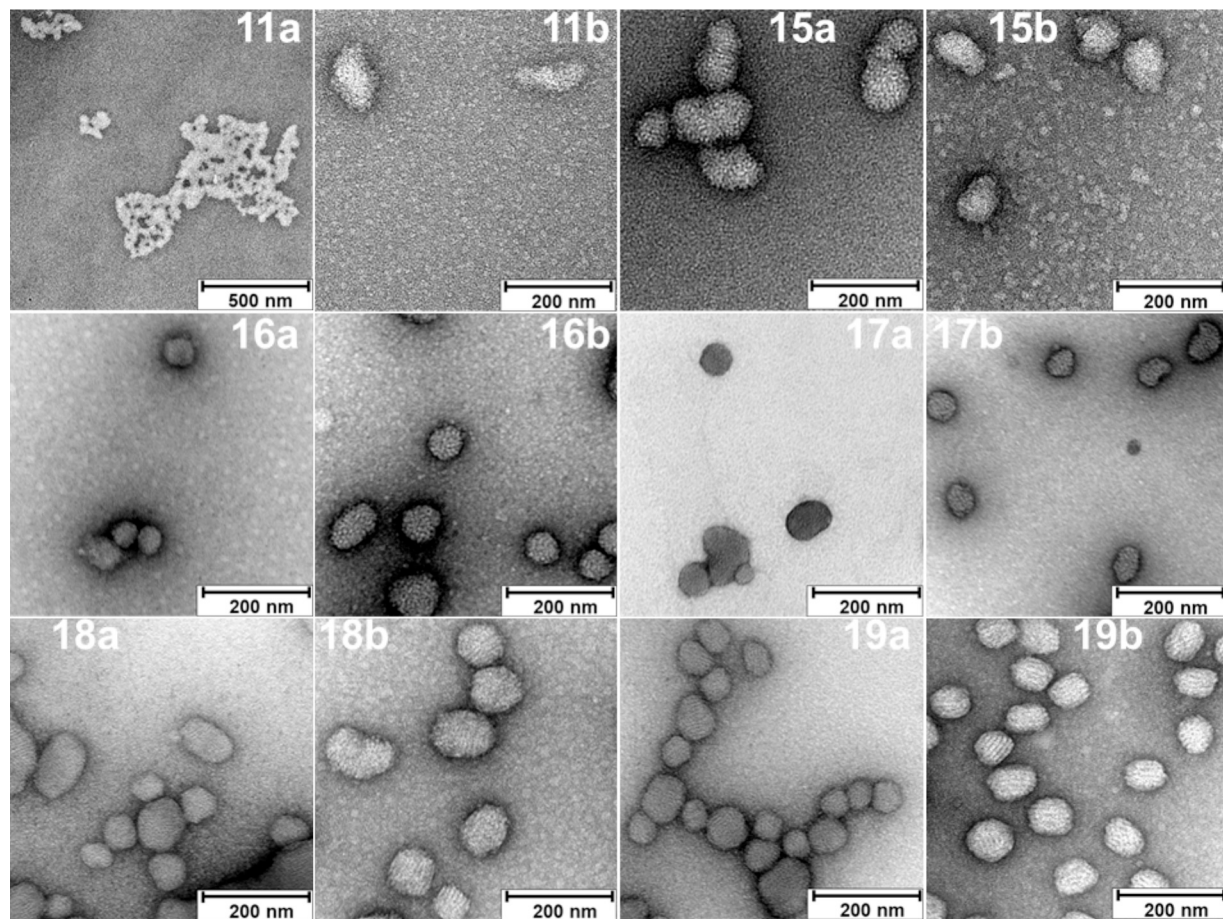


Fig. 4. Representative TEM micrographs of N/P 5 CDplex formulations obtained from compounds 11a,b and 15a,b–19a,b.

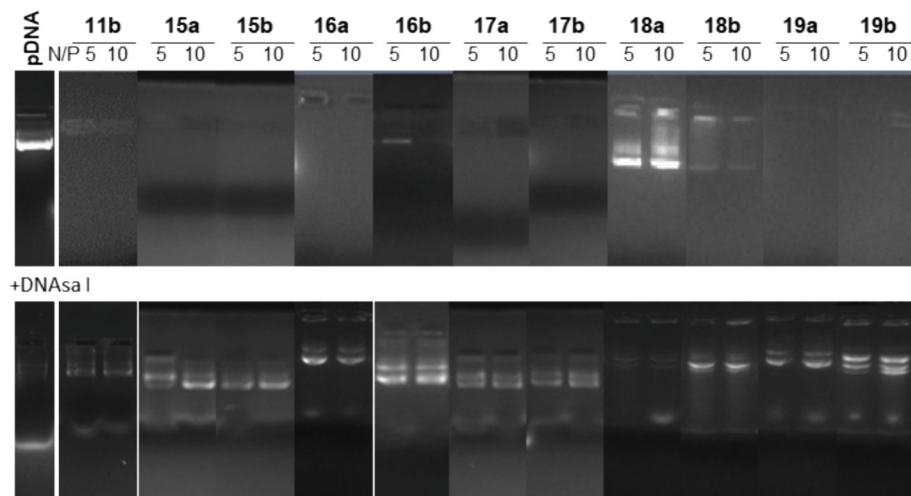


Fig. 5. EMSA gels for nanocomplexes formulated with pDNA (pCMV-Luc VR1216) and the GFAs 11b and 15a,b–19a,b at N/P 5 and 10, before (upper panel) and after treatment with DNase I and subsequent dissociation of the complexes with sodium dodecylsulfate (lower panel); naked pDNA was used as a control.

interactions (Fig. 7B). However, the van der Waals interaction energy was more favorable when the dimer was parallelly oriented to the DNA fragments during the approaching process, probably due to the better accommodation of charged dimer branches in the DNA grooves. The strain energy (the sum of bond stretching, angle bending and torsional energy terms) for the DNA and 15b units in the complex, increases at the shortest distances (Fig. 7C). Balancing all effects, the (15b)₂(DNA)₂ MBE structure was identified (Fig. 7D). In the complex, the DNA—DNA

interactions are almost negligible. In fact, they start to become strongly repulsive below distances of about 3.2 nm. In other words, the charged dimer is necessary to stabilize two nearly parallel DNA fragments.

The (15b)₂(DNA)₂ complex exhibited remarkable stability in this parallel configuration during subsequent MD simulations in explicit water (Fig. 8A). Interestingly, replicating the interaction pattern along a coiled pDNA molecule would result in tubular-like arrangements of the GFA units (Fig. 8B) between quasi-parallel DNA chains, distinct from the

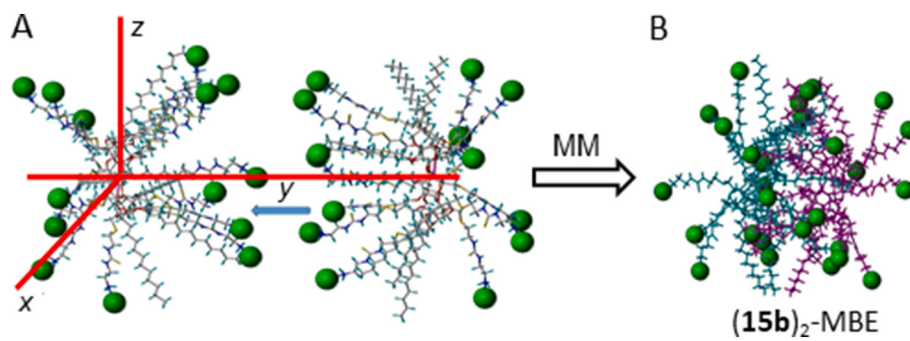


Fig. 6. A) Coordinate system used for a **15b** molecule (right) approaching another **15b** molecule with its center of mass (relative to the glycosidic oxygen atoms) at the origin (left) along the *y* coordinate, in the configuration where the secondary rims of the β CD units are facing (chloride anions in green). B) MBE structure (MM) of the secondary face-to-secondary face **(15b)₂**-dimer.

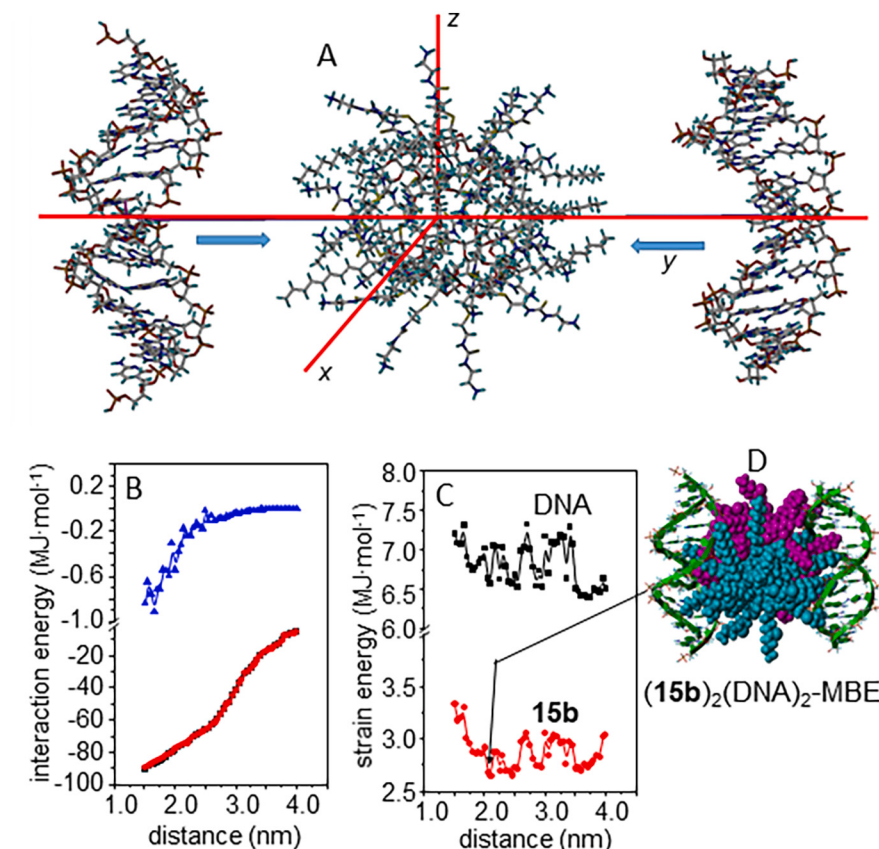


Fig. 7. A) Coordinate system used for the approaching of two equidistant antiparallel DNA fragments to **(15b)₂**-dimer (charged dimer structure obtained from MM and 1 ns MD experiments) along the *y* coordinate; the dimer was located along the *z*-axis, i.e. parallel to the DNA helical fragments. B) Total interaction energies (■, black) and the electrostatics (●, red) and van der Waals (▲, blue) contributions between the DNA fragments and the longitudinally oriented **(15b)₂**-dimer as a function of the average of the distances between the center of mass of the DNA fragments and the dimer; note that the total and the electrostatics interaction energies are almost coincident. C) Strain energy for the DNA fragments (■, black) and the **(15b)₂**-dimer (●, red) as a function of the average of the distances between the center of mass of the two DNA fragments and the dimer. D) MBE structure (MM) of the structure of the **(15b)₂(DNA)₂** complex.

perpendicular arrangement typically seen in complexes from Janus type CD vectors, as depicted in Fig. 1. Ultimately, this configuration leads to cord-like templated alignment of GFA molecules within the plasmid coils will form, effectively reproducing the pupa-like regions observed in GFA CDplexes (Fig. 8C and D).

For the analogous experiment where the MBE **15b**-dimer structure was initially placed with the CD axis of symmetry oriented perpendicularly (along the *y*-axis) to the two parallel DNA fragments, MD simulations revealed the prompt dissociation of the layered complex into individual complexes comprising a single GFA molecule and a single

DNA fragment. Prolonged simulation times revealed complexes in which a single GFA molecule bridged the two DNA fragments, aligning with the anticipated scenario in disordered regions of CDplexes (see the Supplementary data, Figs. S44–S55, for a comprehensive discussion of the computational data). Altogether, the findings from these simulations complement the experimental observations, providing a more comprehensive understanding of the complex interactions occurring within these systems. This insight further supports the notion that the interplay between the molecular components and the structural organization is fundamental in achieving different CDplex architectures.

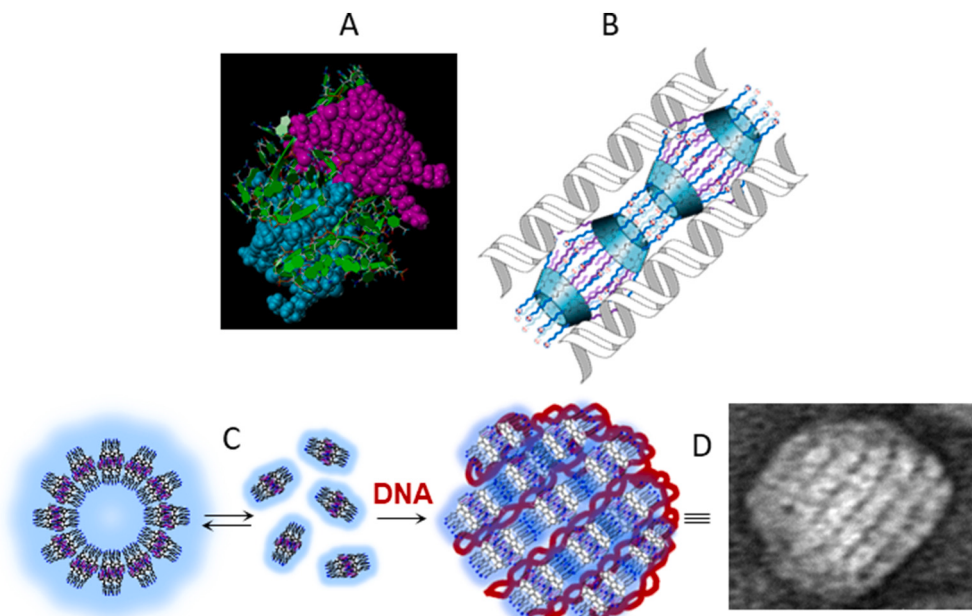


Fig. 8. Upper panel: A) Snapshot of the $(15b)_2(DNA)_2$ complex after a 0.5 s MD simulation in explicit water. B) Schematic representation showing the preferred parallel arrangement of GFA units between DNA chains. Lower panel: Cartoon of the proposed mechanism for the co-assembly of GFAs and pDNA leading to pupa-like arrangements. C) At the close-to-neutral pH of CDplex formulation, GFA bilayer vesicles predominate that, according to computational data, will be in equilibrium with secondary rim-faced dimers. D) Upon formulation, hierarchical co-assembly takes place, whereby coiled DNA serves as template for the alignment of GFA dimers, leading to the characteristic ultrathin pattern with alternating dark (high electron density) and light regions (low electron density) observed in the TEM micrographs.

3.5. Toxicity and *in vitro* cell transfection

Nanocomplexes prepared from the β CD-based GFAs **11b**, **15a,b-17a,b** and **19a,b** and the luciferase-encoding reporter gene pCMV-Luc VR1216, found to exhibit good cargo-protecting capabilities, were subsequently evaluated for their transfection efficiency *in vitro* using African green monkey epithelial kidney COS-7, human hepatocellular carcinoma HepG2, murine macrophage RAW264.7 and newborn porcine tracheal NPT_r cells. All experiments were conducted in the presence of 10 % serum. Polyplexes formed from branched polyethylenimine (bPEI, MW 25 kDa), a widely used cationic polymer for nonviral gene delivery, were also included as controls. Absolute luciferase expression data are presented in Fig. 9A and B (see also Supplementary data, Figs. S56–S59). It is important to note that RAW264.7 cells are known for their higher resistance to transfection in cell culture (Dokka et al., 2000), which complicates direct analysis when evaluating transfection selectivity and drawing correlations between *in vitro* and *in vivo* data. As a result, relative variations in transfection efficiency often become more indicative of underlying trends (Jansig et al., 2020). To ensure meaningful comparisons, the data have been normalized against the luciferase expression value obtained for bPEI/pDNA polyplexes prepared at N/P 10, which represents the optimal conditions for the control, in each cell line (Fig. 9C).

The results revealed distinct impacts of variations in the molecular structure of GFAs on cell transfection selectivity. For example, the inclusion of the thiourea segment in compound **15b**, as opposed to **11b**, occasioned a significant enhancement in transfection efficiency in COS-7 cells compared to HepG2 cells. Conversely, reducing the length of the lipid tail from 12 (**15b**) to 6 carbons (**15a**) led to a marked improvement in transfection levels in HepG2 and NPT_r cells, resulting in CD complexes with a broader spectrum of activity. However, the most significant change was observed with modifications in the cationic domain. Thus, substituting the terminal primary amines in **15a** and **15b** with secondary amines in **16a** and **16b** had a notably detrimental impact across all cell lines. Introducing a combination of tertiary and primary

amines in **17a** and **17b** led to a restoration of transfection levels in COS-7 cells. Remarkably, compounds **19a** and **19b**, featuring hydroxypyridine cationic heads, mediated transfection in RAW264.7 macrophages with significantly higher relative efficiency, surpassing PEI-formulated polyplexes by up to 14-fold.

The transfection efficiency was found to monotonically decreased on going from N/P 5 to N/P 10. This could be attributed to a size effect, as larger particles generally exhibit higher uptake rates by cells cultured *in vitro* (Pezzoli et al., 2017). Notwithstanding, while D_h values follow the same decreasing trend, the differences remain modest (Table 2). Consistent with previous findings (Carbajo-Gordillo et al., 2019), the observed behavior suggests that an excess of the vector forms an external shell and slows release of the pDNA cargo intracellularly.

Cell viability for all *in vitro* tested formulations and cell types was assessed using the AlamarBlue assay (Fig. 10). In COS-7 cells, viability remained above 80 % for most formulations, except for compound **16b**, which features secondary amine cationic heads and dodecyl lipid tails; this compound showed reduced viability of approximately 70 % at N/P 5 and 40 % at N/P 10. In RAW264.7 cells, all N/P 5 formulations maintained viabilities above 80 %. However, increasing the N/P ratio to 10 had a pronounced negative effect in certain cases, notably with compound **16a** ($42 \pm 6\%$) and **19a** ($53 \pm 9\%$). Compound **15b** was particularly toxic to HepG2 cells, with viability dropping to $52 \pm 1\%$ at N/P 5 and $33 \pm 2\%$ at N/P 10. Reduced viability was also observed for **16b** in this cell line when formulated at N/P 10 ($67 \pm 4\%$). No significant viability concerns were observed in NPT_r cells.

This was particularly evident for the nanocomplexes formulated with compounds **16b** in COS-7 cells, compounds **15b** and **16b** in HepG2 cells, and compound **16a** and **19a** in RAW264.7 cells. At N/P 5, only the formulations obtained from **15b** (in HepG2) and **16b** (in COS-7) showed cell viability values below 80 % (Fig. 10).

In order to further explore the potential of the new GFAs for the conception of nucleic acid therapeutics, compounds **19a** and **19b** were next formulated with the plasmid pCMVIL12, which encodes the potent antitumoral cytokine interleukin-12 (IL-12) (Liu et al., 2017), and

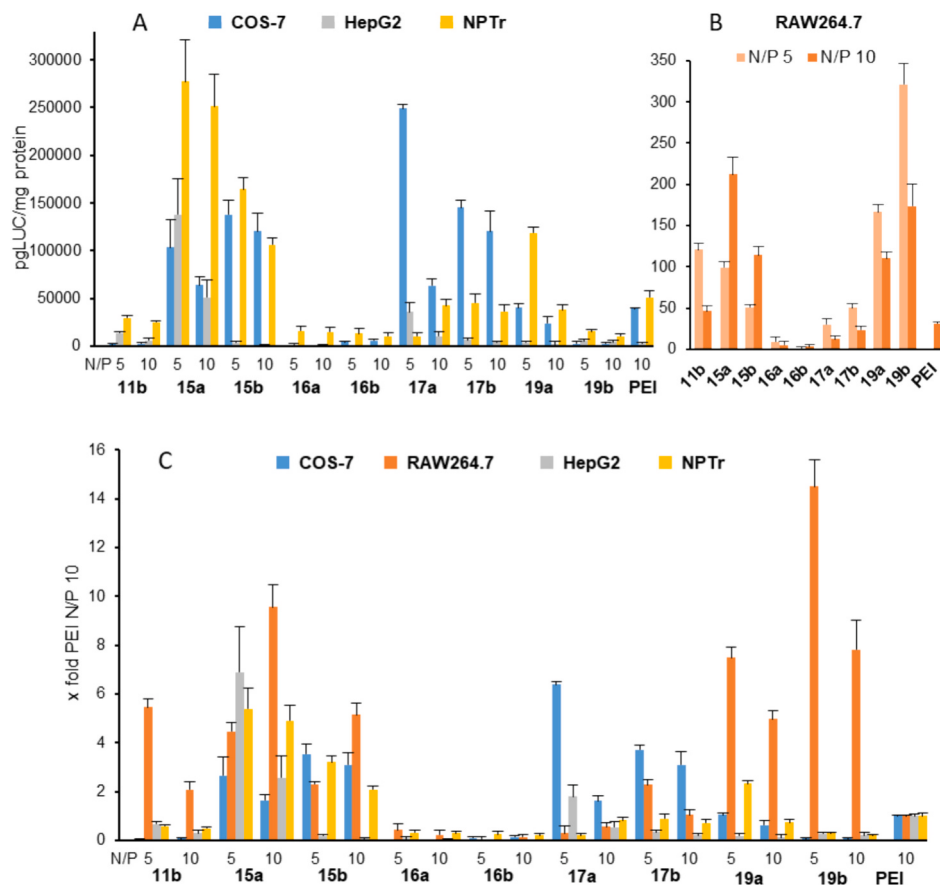


Fig. 9. A) Transfection efficiency in COS-7, HepG2 and NPTr cells for nanocomplexes formulated with the GFAs 11b, 15a,b-17a,b and 19a,b and the luciferase encoding gene pCMV-Luc VR1216 at N/P 5 and 10, in the presence of 10 % fetal bovine serum (FBS). B) Idem for RAW 264.7 cells. C) Relative transfection efficiency data normalized to the value obtained for PEI/pDNA polyplexes (N/P 10) in each cell line. The data represent the mean \pm SD of three wells and are representative of three independent determinations.

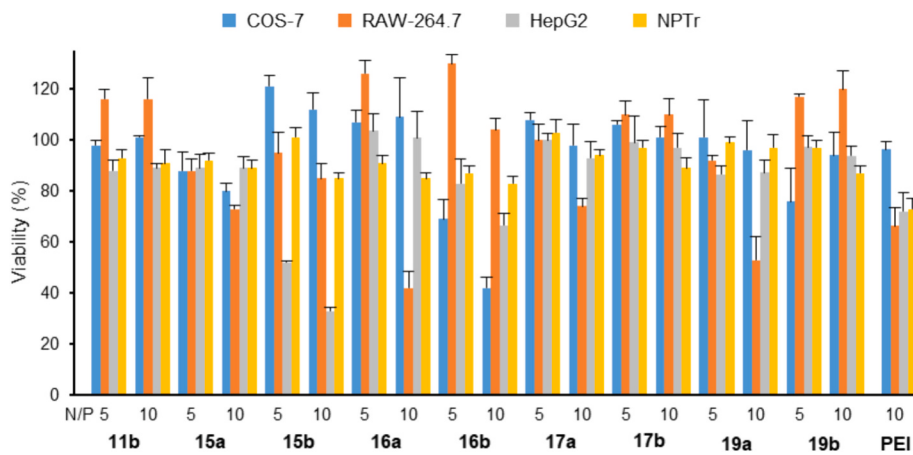


Fig. 10. Viability of COS-7, RAW 264.7, HepG2 and NPTr cells in the presence of nanocomplexes formulated with the GFAs 11b, 15a,b-17a,b and 19a,b and the luciferase encoding gene pCMV-Luc VR1216 at N/P 10, in the presence of 10 % fetal bovine serum (FBS), determined by the AlamarBlue assay. Data for polyplexes formulated with PEI are also shown. The data represent the mean \pm SD of three wells and are representative of three independent determinations.

deliver it into RAW264.7 cells. Gratifyingly, the corresponding nanocomplexes (N/P 5) performed even better than those prepared from the reporter luciferase-encoding plasmid, whereas the control PEI polyplexes did not show any detectable expression of IL12 (Supplementary data, Fig. S60).

3.6. In vivo transfection

Nanoparticle shape, size, and internal structure significantly influence their biodistribution and choice of endocytic pathways, which are crucial for the *in vivo* targeting of molecular vector-based pDNA nanocomplexes. The ability to engineer different nanoscale topologies by customizing the vector architecture at the molecular level, as

demonstrated by the GFA prototype, presents promising opportunities. To evaluate and quantify the efficiency of *in vivo* delivery and the capacity of GFAs to facilitate organ-specific transfection, we conducted experiments using Balb-c mice (8 animals per experiment, consisting of 4 females and 4 males, aged 6–8 weeks, weighting 20–25 g). We selected formulations prepared by combining compounds **15a**, **17a**, **19a**, and **19b** with pCMV-Luc VR1216 pDNA (50 µg) at an N/P ratio of 5, based on their unique cell selectivities and limited toxicities, and administered them *via* tail vein injections (200 µL). Twenty-four hours post-injection, the mice were sacrificed, and luciferase expression was measured in the heart, kidneys, liver, lungs, and spleen following organ homogenization.

Fluorescence was readily apparent in all the analyzed organs of mice treated with **15a**/pDNA CDplexes, which formed ellipsoidal particles with an internal organization dominated by sinusoidal arrangements of interrupted arches. Transfection occurred preferentially at the liver, but it was still significant at the lung. The smaller **17a**/pDNA nanocomplexes, with a less defined core, were globally less efficient, but showed a remarkable selectivity for the kidney. Sharply different, the **19a**/pDNA and **19b**/pDNA N/P 5 formulations, which afford nanoparticles with a very characteristic pupa-like topology, exhibited a marked tropism to the spleen. CDplexes obtained from **19a** were found more efficient in terms of overall transfection level, but spleen selectivity was higher for **19b**, with only residual fluorescence observed in other organs (Fig. 11).

Ascribing the observed variations in relative cell transfection performances *in vitro* and in organ tropisms *in vivo* to a combination of CDplex surface (shape and charge) and internal order divergences is appealing. For instance, the exceptional amplification in transfection of **19a** and **19b** towards the macrophage lineage and the spleen correlates with their distinct GFA/pDNA pupa-like organization. Conversely, the preference for hepatocytes and epithelial cells, correlating with favoured delivery to the liver and the lung, in the case of **15a** can be attributed to the predominant rod-type shape of the corresponding CDplexes. The markedly different transfection outcomes observed for derivatives **16a** and **17a** in the fibroblast cell line, despite their formation of spherical nanocomplexes with similar short-range ordered patterns, may arise instead from dissimilarities in the internal charge, given the differences in the number of cationizable amino groups per arm, the intrinsic pK_a (Fig. 2) and the transition pH value (Table 1). Notably, the later showed high kidney selectivity *in vivo*.

The molecular and co-assembling properties of GFAs are also expected to result in distinct endosomolytic characteristics. As observed in lipid nanoparticles (LNPs), ionizable lipids, once protonated within the acidic environment of the endosome, form ion pairs with anionic lipids in the endosomal membrane (Eygeris et al., 2022). This interaction leads to the formation of an inverse hexagonal phase, which disrupts the endosomal membrane and facilitates the release of the nucleic acid

cargo into the cytosol, thereby enabling transfection. The endosomal disruption capabilities of different ionizable lipids vary based on their structural properties, and are particularly enhanced when tertiary amino groups are present (Philipp et al., 2023). This is the case for GFAs **17a,b** and **19a,b**. The efficiency of this process may also vary between cell types, potentially contributing to the selectivity observed in both *in vitro* and *in vivo*.

A second hypothesis for explaining the endogenous cell and organ targeting mechanism of CDplexes involves the adsorption of specific proteins to the CDplex surface, resulting in unique dynamic coatings. It is important to note that serum proteins rapidly adhere to the surface of administered nanoparticles, forming an interfacial layer known as the “protein corona,” which defines their biological identity. By comparing *in vitro* cell transfection data with *in vivo* organ targeting results, we observe that increased efficiency in HepG2 hepatocytes and NPTr epithelial cells (for **15a**), COS-7 fibroblasts (for **17a**), and RAW264.7 macrophages (for **19a** and **19b** formulations) corresponds to preferential delivery to the liver and lung, kidney and heart, or spleen, respectively. This suggests that different sets of serum proteins bind to various GFA-pDNA assemblies, potentially interacting with specific receptors on target cells to enhance cellular uptake and promote intracellular pDNA delivery. The concept of endogenous targeting *via* serum proteins has been recently demonstrated for LNP systems (Dilliard et al., 2021) and may be applicable here as well (Martínez-Negro et al., 2017). For example, apolipoprotein E (ApoE) facilitates LNP uptake by liver hepatocytes through the low-density lipoprotein receptor (LDL-R), β -glycoprotein I (β 2-GPI) binds to phosphatidylserine-containing vesicles or apoptotic cells, promoting macrophage engulfment and spleen filtration, and vitronectin (Vtn) could bind its receptor, α v β 3 integrin, which is highly expressed in the pulmonary endothelium but not in liver cells or other vascular beds. Similarly, very low-density lipoproteins (VLDLs) may mediate fibroblast internalization *via* the VLDL receptor (VLDLR) (Go & Mani, 2012).

It is likely that all the potential mechanisms discussed above contribute to the observed experimental outcomes, making it challenging to establish clear correlations between *in vitro* and *in vivo* results. For example, enhanced cellular uptake does not necessarily lead to more efficient cargo delivery. Additionally, the composition of the protein corona is known to change significantly between *in vitro* and *in vivo* environments (Singh et al., 2021), and even between different biological fluids, such as plasma and cerebrospinal fluid. This suggests that the site of administration could impact LNP efficacy *in vivo* (van Straten et al., 2024). The variability in transfection efficiency across different cell lines may reflect inherent differences in endocytic processes or endosomal escape mechanisms, influenced by a combination of cellular and vector-related factors (Smith et al., 2019).

4. Conclusions

The ensemble of data provides conclusive evidence on the strong potential of judiciously installing different arrangements of functional elements onto a β CD core to efficiently access perfectly monodisperse GFAs with tailored structures and properties beyond the Janus archetype. The synthetic scheme takes advantage of the higher reactivity of the OH6 and OH2 hydroxyl sets in base-promoted alkylation reactions as compared to the OH3 hydroxyls, enabling a straight forward, scalable access to sequence-defined tetradecaallylated precursors. A sequential combination of metal-free thiol-ene and thiourea-forming click-type reactions allows then installing a variety of cationic heads covering an intrinsic pK_a range of 6.4 to 10.7. A collection of perfectly monodisperse GFA materials for structure-self-assembly-DNA nanocondensation-transfection efficiency and selectivity relationship studies was thus accessed.

All compounds exhibited pH-dependent transitions in aqueous medium involving, generally, the formation of lipid bilayers that dissociate into individual molecules as the acidity increases. In the presence of

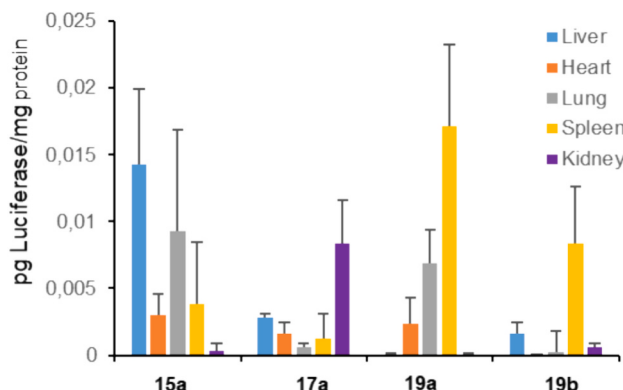


Fig. 11. Gene expression conducted *in vivo* after intravenous administration of 50 µg of pCMV-Luc VR1216 formulated with **15a**, **17a**, **19a** and **19b** at N/P 5. Bars represent the mean \pm SD ($n = 8$ animals).

pDNA, nanocomplexes with varied topologies were formed. Notable differences in their internal order were also evidenced by TEM. Short range order preferentially involves interactions of individual molecules with the oligonucleotide chain. Conversely, long-range order, particularly pupa-like arrangements, can be rationalized in terms of pDNA-templated longitudinal alignment of face-to-face GFA dimers, which can be considered the basic constituent of lipid bilayers. *In vitro* and *in vivo* evaluation of the transfection efficiency revealed striking cell and organ selectivity patterns that can be correlated with specific nanocomplex topologies. Remarkably, pupa-like nanocomplexes exhibited a clear preference for RAW264.7 macrophages, considered to be rather refractory to transfection, that correlated with a marked tropism to the spleen. The intriguing overlap of cell linages and tissue targets strongly suggests that receptor-mediated mechanisms, issued from preferential adsorption of distinct serum proteins on the particle surface, might operate to a certain extent. Nevertheless, the contribution of nanocomplex topology and protein corona composition to the *in vitro* and *in vivo* transfection mechanisms of GFA-based nanoparticles needs experimental validation, and it is essential to be cautious about making any generalizations.

Despite this, the results collectively highlight cyclodextrin-based GFAs as a promising class of molecular vectors capable of finely tuning cell and organ transfection selectivity through precise chemical engineering.

Abbreviations

CD	cyclodextrin
DLS	dynamic light scattering
EDTA	ethylenediaminetetraacetic acid
TFA	trifluoroacetic acid
GFA	geometrically frustrated amphiphile
HEPES	4-(2-hydroxyethyl)-1-piperazineethanesulfonic acid
bPEI	branched poly-(ethylenimine)
MBE	minima binding energy
MD	molecular dynamics
MM	molecular mechanics
MNP	molecular nanoparticle
pDNA	plasmid DNA
SD	standard deviation
SDS	sodium dodecyl sulfate
SLS	static light scattering
TEM	transmission electron microscopy

CRediT authorship contribution statement

Gonzalo Rivero-Barbarroja: Writing – review & editing, Methodology, Investigation, Formal analysis. **José López-Fernández:** Writing – review & editing, Methodology, Investigation. **Inmaculada Juárez-González:** Writing – review & editing, Methodology, Investigation, Formal analysis. **Carlos Fernández-Clavero:** Writing – review & editing, Methodology, Investigation, Formal analysis. **Christophe Di Giorgio:** Writing – review & editing, Validation, Methodology, Investigation, Formal analysis. **Itziar Vélaz:** Writing – review & editing, Validation, Supervision, Investigation. **María J. Garrido:** Writing – review & editing, Validation, Supervision, Investigation. **Juan M. Benito:** Writing – review & editing, Validation, Supervision, Investigation, Funding acquisition. **Carmen Ortiz Mellet:** Writing – review & editing, Writing – original draft, Supervision, Funding acquisition, Conceptualization. **Francisco Mendicutí:** Writing – review & editing, Writing – original draft, Supervision, Funding acquisition, Conceptualization. **Conchita Tros de Ilarduya:** Writing – review & editing, Writing – original draft, Supervision, Funding acquisition, Conceptualization. **José M. García Fernández:** Writing – review & editing, Writing – original draft, Supervision, Resources, Funding acquisition, Conceptualization.

Declaration of competing interest

The authors declare no competing financial interest.

Acknowledgements

We acknowledge the Ministerio de Ciencia, Innovación y Universidades and the Agencia Estatal de Investigación, AEI/10.13039/501100011033 and “ERDF A way of making Europe” (PID2020-118384GB-I00, PID2021-124247OB-C21, PID2021-124247OB-C22 and PID2022-141034OB-C21) and the CAM (CM/JIN/2021-022). We also acknowledge funding by the European Union’s Horizon Europe research and innovation programme under the Marie Skłodowska-Curie grant agreement 101130235 – Bicyclós and the PTI+ Global Health (CSIC). The CITIUS (Univ. Seville) is additionally acknowledged for technical support. G.R.-B and J. L.-F. (Grant numbers FPU18/02922 and PRE2019-088271, respectively). C.F.-C. thanks the UAH collaboration grant awarded.

Appendix A. Supplementary data

Detailed general methods and instruments, synthetic procedures, compound characterization, copies of the NMR and MS spectra, nanocomplex properties, computational studies (PDF) and absolute *in vitro* transfection and cell viability data. Supplementary data to this article can be found online at <https://doi.org/10.1016/j.carbpol.2024.122776>.

References

- Aranda, C., Urbiola, K., Mendez-Ardoy, A., García Fernández, J. M., Ortiz Mellet, C., & Tros de Ilarduya, C. (2013). Targeted gene delivery by new folate-polycationic amphiphilic cyclodextrin-DNA nanocomplexes *in vitro* and *in vivo*. *European Journal of Pharmaceutics and Biopharmaceutics*, 85, 390–397. <https://doi.org/10.1016/j.ejpb.2013.06.011>
- Bagnacani, V., Franceschi, V., Bassi, M., Lomazzi, M., Donofrio, G., Sansone, F., Casnati, A., & Ungaro, R. (2013). Arginine clustering on calix[4]arene macrocycles for improved cell penetration and DNA delivery. *Nature Communications*, 4, 1721. <https://doi.org/10.1038/ncomms2721>
- Berner-Kowollik, C., Du Prez, F. E., Espeel, P., Hawker, C. J., Junkers, T., Schlaad, H., & Van Camp, W. (2011). “Clicking” polymers or just efficient linking: What is the difference? *Angewandte Chemie International Edition*, 50(1), 60–62. <https://doi.org/10.1002/anie.201003707>
- Barrán-Berdón, A. L., B. Yélamos, B., García-Rio, L., Domenech, O., Aicart, E., & Junquera, E. (2015). Polycationic macrocyclic scaffolds as potential non-viral vectors of DNA: A multidisciplinary study. *ACS Applied Materials & Interfaces*, 7(26), 14404–14414. <https://doi.org/10.1021/acsm.5b03231>
- Bartolami, E., Bessin, Y., Gervais, V., Dumy, P., & Ulrich, S. (2015). Dynamic expression of DNA complexation with self-assembled biomolecular clusters. *Angewandte Chemie International Edition*, 54(35), 10183–10187. <https://doi.org/10.1002/anie.201504047>
- Benito, J. M., Gómez-García, M., Ortiz Mellet, C., Baussanne, I., Defaye, J., & García Fernández, J. M. (2004). Optimizing saccharide-directed molecular delivery to biological receptors: Design, synthesis, and biological evaluation of glycodendrimer–cyclodextrin conjugates. *Journal of the American Chemical Society*, 126(33), 10355–10363. <https://doi.org/10.1021/ja047864v>
- Bienvenu, C., Martínez, A., Jiménez Blanco, J. L., Di Giorgio, C., Vierling, P., Ortiz Mellet, C., ... García Fernández, J. M. (2012). Polycationic amphiphilic cyclodextrins as gene vectors: Effect of the macrocyclic ring size on the DNA complexing and delivery properties. *Organic & Biomolecular Chemistry*, 10(29), 5570–5581. <https://doi.org/10.1039/C2OB25786F>
- Bigini, P., Gobbi, M., Bonati, M., Clavenna, A., Zucchetti, M., Garattini, S., & Pasut, G. (2021). The role and impact of polyethylene glycol on anaphylactic reactions to COVID-19 nano-vaccines. *Nature Nanotechnology*, 16(11), 1169–1171. <https://doi.org/10.1038/s41565-021-01001-3>
- Bijelic, A., Aureliano, M., & Rompel, A. (2019). Polyoxometalates as potential next-generation metallodrugs in the combat against cancer. *Angewandte Chemie International Edition*, 58(10), 2980–2999. <https://doi.org/10.1002/anie.201803868>
- Blanco, M. (1991). Molecular silverware. I. General solutions to excluded volume constrained problems. *Journal of Computational Chemistry*, 12(2), 237–247. <https://doi.org/10.1002/jcc.540120214>
- Blenke, E. O., Örnskov, E., Schöneich, C., Nilsson, G. A., Volkin, D. B., Mastrobattista, E., ... Crommelin, D. J. A. (2023). The storage and in-use stability of mRNA vaccines and therapeutics: Not a cold case. *Journal of Pharmaceutical Sciences*, 112(2), 386–403. <https://doi.org/10.1016/j.xphs.2022.11.001>
- Borisov, O. V., Zhulina, E. B., Leermakers, F. A. M., & Müller, A. H. E. (2011). Self-assembled structures of amphiphilic ionic block copolymers: Theory, self-consistent

- field modeling and experiment. *Advances in Polymer Science*, 241, 57–129. https://doi.org/10.1007/12_2011_114
- Breton, M., Leblond, J., Tranchant, I., Scherman, D., Bessodes, M., Herscovici, J., & Mignet, N. (2011). Lipothioureas as lipids for gene transfection: A review. *Pharmaceuticals*, 4(10), 1381–1399. <https://doi.org/10.3390/ph4101381>
- Brunel, Y., Faucher, H., Gagnaire, D., & Rassat, A. (1975). Programme de minimisation de l'énergie empirique d'une molécule par une méthode simpliciale. *Tetrahedron*, 31 (8), 1075–1091. [https://doi.org/10.1016/0040-4020\(75\)80129-3](https://doi.org/10.1016/0040-4020(75)80129-3)
- Bulcha, J. T., Wang, Y., Ma, H., Tai, P. W. L., & Gao, G. (2021). Viral vector platforms within the gene therapy landscape. *Signal Transduction and Targeted Therapy*, 6, 53. <https://doi.org/10.1038/s41392-021-00487-6>
- Carbajo-Gordillo, A. I., González-Cuesta, M., Jiménez Blanco, J. L., Benito, J. M., Santana-Armas, M. L., Carmona, T., ... García Fernández, J. M. (2021). Trifaceted Mickey mouse amphiphiles for programmable self-assembly, DNA complexation and organ-selective gene delivery. *Chemistry A European Journal*, 27(36), 9429–9438. <https://doi.org/10.1002/chem.202100832>
- Carbajo-Gordillo, A. I., Jiménez Blanco, J. L., Benito, J. M., Lana, H., Marcelo, G., Di Giorgio, C., ... García Fernández, J. M. (2020). Click synthesis of size- and shape-tunable star polymers with functional macrocyclic cores for synergistic DNA complexation and delivery. *Biomacromolecules*, 21(12), 5173–5188. <https://doi.org/10.1021/acs.biomac.0c01283>
- Carbajo-Gordillo, A. I., López-Fernández, J., Benito, J. M., Jiménez Blanco, J. L., Santana-Armas, M. L., Marcelo, G., ... García Fernández, J. M. (2022). Enhanced gene delivery triggered by dual pH/redox responsive host-guest dimerization of cyclooligosaccharide star polycations. *Macromolecular Rapid Communications*, 43 (11), Article 2200145. <https://doi.org/10.1002/marc.202200145>
- Carbajo-Gordillo, A. I., Rodríguez-Lavado, J., Jiménez Blanco, J. L., Benito, J. M., Di Giorgio, C., Vélez, I., ... García Fernández, J. M. (2019). Trehalose-based Siamese twin amphiphiles with tunable self-assembling, DNA nanocomplexing and gene delivery properties. *Chemical Communications*, 55(57), 8227–8230. <https://doi.org/10.1039/C9CC04489B>
- Cheng, Q., Wei, T., Farbiak, L., Johnson, L. T., Dilliard, S. A., & Siegwart, D. J. (2020). Selective organ targeting (SORT) nanoparticles for tissue-specific mRNA delivery and CRISPR-Cas gene editing. *Nature Nanotechnology*, 15(4), 313–320. <https://doi.org/10.1038/s41565-020-0669-6>
- Chernikova, E. Y., & Berdnikova, D. V. (2020). Cucurbiturils in nucleic acids research. *Chemical Communications*, 56(98), 15360–15376. <https://doi.org/10.1039/D0CC06583H>
- Chung, Y. H., Beiss, V., Fiering, S. N., & Steinmetz, N. F. (2020). COVID-19 vaccine frontrunners and their nanotechnology design. *ACS Nano*, 14(10), 12522–12537. <https://doi.org/10.1021/acsnano.0c.accounts.9b00368>
- Clark, M., Cramer, R. D., III, & Van Opdenbosch, N. (1989). Validation of the general purpose Tripos 5.2 force field. *Journal of Computational Chemistry*, 10(8), 982–1012. <https://doi.org/10.1002/jcc.540100804>
- Cullis, P. R., & Hope, M. J. (2017). Lipid nanoparticle systems for enabling gene therapies. *Molecular Therapy*, 25(7), 1467–1475. <https://doi.org/10.1016/j.mtymthe.2017.03.013>
- de Vrieze, J. (2021). Pfizer's vaccine raises allergy concerns. *Science*, 371(6524), 10–11. <https://doi.org/10.1126/science.371.6524.10>
- Díaz-Moscoso, A., Guilloteau, N., Bienvenu, C., Mendez-Ardoy, A., Blanco, J. L., Benito, J. M., ... García Fernández, J. M. (2011). Mannosyl-coated nanocomplexes from amphiphilic cyclodextrins and pDNA for site-specific gene delivery. *Biomaterials*, 32(29), 7263–7273. <https://doi.org/10.1016/j.biomaterials.2011.06.025>
- Díaz-Moscoso, A., Le Gourriérec, L., Gómez-García, M., Benito, J. M., Balbuena, P., Ortega-Caballero, F., ... García Fernández, J. M. (2009). Polycationic amphiphilic cyclodextrins for gene delivery: Synthesis and effect of structural modifications on plasmid DNA complex stability, cytotoxicity, and gene expression. *Chemistry A European Journal*, 15(46), 12871–12888. <https://doi.org/10.1002/chem.200901149>
- Dilliard, S. A., Chenga, Q., & Siegwart, D. J. (2021). On the mechanism of tissue-specific mRNA delivery by selective organ targeting nanoparticles. *Proceedings of the National Academy of Sciences USA*, 118, Article e2109256118. <https://doi.org/10.1073/pnas.2109256118>
- Dilliard, S. A., & Siegwart, D. J. (2023). Passive, active and endogenous organ-targeted lipid and polymer nanoparticles for delivery of genetic drugs. *Nature Reviews Materials*, 8(4), 282–300. <https://doi.org/10.1038/s41578-022-00529-7>
- Ding, P., Yin, X., Wang, Q., Kang, X., Wu, M., Zhu, K., Wang, X., Wang, R., & Xue, G. (2020). Open and closed layered nanostructures with sub-10 nm periodicity self-assembled from hydrophilic [60]fullerene-based giant surfactants. *Langmuir*, 36(26), 7289–7295. <https://doi.org/10.1021/acs.langmuir.0c00659>
- Dokka, S., Toledo, D., Shi, X., Ye, J., & Rojanasakul, Y. (2000). High-efficiency gene transfection of macrophages by lipoplexes. *International Journal of Pharmaceutics*, 206(1–2), 97–104. ISSN [https://doi.org/10.1016/S0378-5173\(00\)00531-7](https://doi.org/10.1016/S0378-5173(00)00531-7)
- Dong, L., Li, Y., Cong, H., Bing Yu, B., & Shen, Y. (2024). A review of chitosan in gene therapy: Developments and challenges. *Carbohydrate Polymers*, 324, Article 121562.
- Dunbar, C. E., High, K. A., Joung, K. J., Kohn, D. B., Ozawa, K., & Sadelain, M. (2018). Gene therapy comes of age. *Science*, 359(6372), Article eaan4672. <https://doi.org/10.1126/science.aan4672>
- Eskandani, Z., Huin, C., & Guégan, P. (2011). Regioselective allylation of cyclomaltoheptaose (β -cyclodextrin) leading to per(2,6-di-O-hydroxypropyl-3-O-methyl)- β -cyclodextrin. *Carbohydrate Research*, 346(15), 2414–2420. <https://doi.org/10.1016/j.carres.2011.08.033>
- Eyeris, Y., Gupta, M., Kim, J., & Sahay, G. (2022). Chemistry of lipid nanoparticles for RNA delivery. *Accounts of Chemical Research*, 55(1), 2–12. <https://doi.org/10.1021/acs.accounts.1c00544>
- Frisch, M. J., Trucks, G. W., Schlegel, H. B., Scuseria, G. E., Robb, M. A., Cheeseman, J. R., ... Fox, D. J. (2009). *Gaussian 09, Revision A* (1st ed.). Wallingford CT: Gaussian, Inc.
- Gallego-Yerga, L., Benito, J. M., Blanco-Fernández, L., Martínez-Negro, M., Vélaz, I., Aicart, E., ... García Fernández, J. M. (2018). Plasmid-templated control of DNA–cyclodextrin nanoparticle morphology through molecular vector design for effective gene delivery. *Chemistry A European Journal*, 24(15), 3825–3835. <https://doi.org/10.1002/chem.201705723>
- Gallego-Yerga, L., González-Alvarez, M. J., Mayordomo, N., Santoyo-González, F., Benito, J. M., Ortiz Mellet, C., ... García Fernández, J. M. (2014). Dynamic self-assembly of polycationic clusters based on cyclodextrins for pH-sensitive DNA nanococondensation and delivery by component design. *Chemistry A European Journal*, 20(22), 6622–6627. <https://doi.org/10.1002/chem.201402026>
- Gallego-Yerga, L., Lomazzi, M., Franceschi, V., Sansone, F., Ortiz Mellet, C., Donofrio, G., ... García Fernández, J. M. (2015). Cyclodextrin- and calixarene-based polycationic amphiphiles as gene delivery systems: A structure-activity relationship study. *Organic & Biomolecular Chemistry*, 13(6), 1708–1723. <https://doi.org/10.1039/C4OB02204A>
- García Fernández, J. M., & Ortiz Mellet, C. (2000). Chemistry and developments of *N*-thiocarbonyl carbohydrate derivatives: Sugar isothiocyanates, thioamides, thioureas, thiocarbamates, and their conjugates. *Advances in Carbohydrate Chemistry and Biochemistry*, 55, 35–135. [https://doi.org/10.1016/S0065-2318\(00\)55004-5](https://doi.org/10.1016/S0065-2318(00)55004-5)
- Gasteiger, J., & Marsili, M. (1980). Iterative partial equalization of orbital electronegativity—A rapid access to atomic charges. *Tetrahedron*, 36(22), 3219–3228. [https://doi.org/10.1016/0040-4020\(80\)80168-2](https://doi.org/10.1016/0040-4020(80)80168-2)
- Gasteiger, J., & Marsili, M. (1987). A new model for calculating atomic charges in molecules. *Tetrahedron Letters*, 19(34), 3181–3184. [https://doi.org/10.1016/S0040-4039\(01\)94977-9](https://doi.org/10.1016/S0040-4039(01)94977-9)
- Geng, W.-C., Huang, Q., Xu, Z., Wang, R., & Guo, D.-S. (2019). Gene delivery based on macrocyclic amphiphiles. *Theranostics*, 9(11), 3094–3106. <https://www.thno.org/v09p3094.htm>
- Go, G.-W., & Mani, A. (2012). Low-density lipoprotein receptor (LDLR) family orchestrates cholesterol homeostasis. *Yale Journal of Biology and Medicine*, 85(1), 19–28. <https://www.ncbi.nlm.nih.gov/pmc/articles/PMC3313535/>
- Gooding, M., Malhotra, M., McCarthy, D. J., Godinho, B. M. D. C., Cryan, J. F., Darcy, R., & O'Driscoll, C. M. (2015). Synthesis and characterization of rabies virus glycoprotein-tagged amphiphilic cyclodextrins for siRNA delivery in human glioblastoma cells: In vitro analysis. *European Journal of Pharmaceutical Sciences*, 71, 80–92. <https://doi.org/10.1016/j.ejps.2015.02.007>
- Guo, J., Ogier, J. R., Desgranges, S., Darcy, R., & O'Driscoll, C. (2012). Anisamide-targeted cyclodextrin nanoparticles for siRNA delivery to prostate tumours in mice. *Biomaterials*, 33(31), 7775–7784. <https://doi.org/10.1016/j.biomaterials.2012.07.012>
- Haley, R. M., Gottardi, R., Langer, R., & Mitchell, M. J. (2020). Cyclodextrins in drug delivery: Applications in gene and combination therapy. *Drug Delivery and Translational Research*, 10(3), 661–677. <https://doi.org/10.1007/s13346-020-00724-5>
- Hatakeyama, H., Akita, H., & Harashima, H. (2011). A multifunctional envelope type nano device (MEND) for gene delivery to tumours based on the EPR effect: A strategy for overcoming the PEG dilemma. *Advanced Drug Delivery Reviews*, 63(3), 152–160. <https://doi.org/10.1016/j.addr.2010.09.001>
- Hofmann, A. M., Wurm, F., & Frey, H. (2011). Rapid access to polyfunctional lipids with complex architecture via oxanyonion ring-opening polymerization. *Macromolecules*, 44(12), 4648–4657. <https://doi.org/10.1021/ma200367c>
- Hou, X., Zaks, T., Langer, R., & Dong, Y. (2021). Lipid nanoparticles for mRNA delivery. *Nature Reviews Materials*, 6(12), 1078–1094. <https://doi.org/10.1038/s41578-021-00358-0>
- Jansig, E., Geissler, S., Rieckmann, V., Kuenemund, A., Hietel, B., Schenk, M., Wussow, S., Kreideweiss, P., Panzner, S., Reinsch, C., & Cynis, H. (2020). Viromers as carriers for mRNA-mediated expression of therapeutic molecules under inflammatory conditions. *Scientific Reports*, 10, 15090. <https://doi.org/10.1038/s41598-020-72004-8>
- Jia, Y., Wang, X., Li, L., Li, F., Zhang, J., & Liang, X.-J. (2024). Lipid nanoparticles optimized for targeting and release of nucleic acid. *Advanced Materials*, 36(4), Article 2305300. <https://doi.org/10.1002/adma.202305300>
- Jiménez Blanco, J. L., Benito, J. M., Ortiz Mellet, C., & García Fernández, J. M. (1999). Sugar thioureas as anion receptors. Effect of intramolecular hydrogen bonding in the carboxylate binding properties of symmetric sugar thioureas. *Organic Letters*, 1(8), 1217–1220. <https://doi.org/10.1021/o1990889s>
- Jiménez Blanco, J. L., Benito, J. M., Ortiz Mellet, C., & García Fernández, J. M. (2017). Molecular nanoparticle-based gene delivery systems. *Journal of Drug Delivery Science and Technology*, 42(1), 18–37. <https://doi.org/10.1016/j.jddst.2017.03.012>
- Jiménez Blanco, J. L., Ortega-Caballero, F., Blanco-Fernández, L., Carmona, T., Marcelo, G., Martínez-Negro, M., ... García Fernández, J. M. (2016). Trehalose-based Janus cyclooligosaccharides: The “click” synthesis and DNA-directed assembly into pH-sensitive transfectious nanoparticles. *Chemical Communications*, 52(66), 10117–10120. <https://doi.org/10.1039/C6CC04791B>
- Kaiser, J. (2018). Gene therapy field hit by fresh safety concern. *Science*, 359(6376), 621. <https://doi.org/10.1126/science.359.6376.621>
- Kali, G., Haddadzadegan, S., & Bernkop-Schnürch, A. (2024). Cyclodextrins and derivatives in drug delivery: New developments, relevant clinical trials, and advanced products. *Carbohydrate Polymers*, 324, Article 121500. <https://doi.org/10.1016/j.carbpol.2023.121500>
- Kazemzadeh, H., & Mozafari, M. (2019). Fullerene-based delivery systems. *Drug Discovery Today*, 24(3), 898–905. <https://doi.org/10.1016/j.drudis.2019.01.013>

- Kim, T., Kim, Y.-J., Han, I.-H., Lee, D., Ham, J., Kang, K. J., & Lee, J. W. (2015). The synthesis of sulforaphane analogues and their protection effect against cisplatin induced cytotoxicity in kidney cells. *Bioorganic & Medicinal Chemistry Letters*, 25(1), 62–66. <https://doi.org/10.1016/j.bmcl.2014.11.014>
- Köstereli, Z., & Severin, K. (2012). Fluorescence sensing of spermine with a frustrated amphiphile. *Chemical Communications*, 48(47), 5841–5843. <https://doi.org/10.1039/C2CC32228E>
- Kulkarni, J. A., Darjuan, M. M., Mercer, J. E., Chen, S., van der Meel, R., Thewalt, J. L., ... Cullis, P. R. (2018). On the formation and morphology of lipid nanoparticles containing ionizable cationic lipids and siRNA. *ACS Nano*, 12(5), 4787–4795. <https://doi.org/10.1021/acsnano.8b01516>
- Kulkarni, J. A., Witzigmann, D., Chen, S., Cullis, P. R., & van der Meel, R. (2019). Lipid nanoparticle technology for clinical translation of siRNA therapeutics. *Accounts of Chemical Research*, 52(9), 2435–2444. <https://doi.org/10.1021/acs.accounts.9b00368>
- Liu, Q., Zhang, T.-X., Zheng, Y., Wang, C., Kang, Z., Zhao, Y., Chai, J., Li, H.-B., Guo, D.-S., Liu, Y., & Shi, L. (2021). Calixarene-embedded nanoparticles for interference-free gene-drug combination cancer therapy. *Small*, 17(8), Article 2006223. <https://doi.org/10.1002/smll.202006223>
- Liu, S., Cheng, Q., Wei, T., Yu, X., Johnson, L. T., Farbiak, L., & Siegwart, D. J. (2021). Membrane destabilizing ionizable phospholipids for organ-selective mRNA delivery and CRISPR-Cas gene editing. *Nature Materials*, 20(5), 701–710. <https://doi.org/10.1038/s41563-020-00886-0>
- Liu, X., Gao, X., Zheng, S., Wang, B., Li, Y., Zhao, C., Muftuoglu, Y., Chen, S., Li, Y., Yao, H., Sun, H., Mao, Q., You, C., Guo, G., & Wei, Y. (2017). Modified nanoparticle mediated IL-12 immunogene therapy for colon cancer. *Nanomedicine*, 13(6), 1993–2004. <https://doi.org/10.1016/j.nano.2017.04.006>
- Lostalé-Seijo, I., & Montenegro, J. (2018). Synthetic materials at the forefront of gene delivery. *Nature Reviews Chemistry*, 2(10), 258–277. <https://doi.org/10.1038/s41570-018-0039-1>
- Ma, S., Hu, Y., & Wang, R. (2015). Self-assembly of polymer tethered molecular nanoparticle shape amphiphiles in selective solvents. *Macromolecules*, 48(9), 3112–3120. <https://doi.org/10.1021/ma5026219>
- Manchón-Corvo, P., & Martín-Duque, P. (2006). Viral gene therapy. *Clinical and Translational Oncology*, 8(12), 858–867. <https://doi.org/10.1007/s12094-006-0149-y>
- Manzanares, D., Araya-Durán, I., Gallego-Yerga, L., Játiva, P., Márquez-Miranda, V., Canan, J., ... Ceña, V. (2017). Molecular determinants for cyclooligosaccharide-based nanoparticle-mediated effective siRNA transfection. *Nanomedicine*, 12(13), 1607–1621. <https://doi.org/10.2217/nmm-2017-0123>
- Martínez-Negro, M., Caracciolo, G., Palchetti, S., Pozzi, D., Capriotti, A. L., Cavaliere, C., ... Junquera, E. (2017). Biophysics and protein corona analysis of Janus cyclodextrin-DNA nanocomplexes. Efficient cellular transfection on cancer cells. *Biochimica et Biophysica Acta - General Subjects*, 1861(7), 1737–1749. <https://doi.org/10.1016/j.bbagen.2017.03.010>
- McMahon, A., O'Neill, M. J., Gómez, E., Donohue, R., Forde, D., Darcy, R., & O'Driscoll, C. M. (2012). Targeted gene delivery to hepatocytes with galactosylated amphiphilic cyclodextrins. *Journal of Pharmacy and Pharmacology*, 64(8), 1063–1073. <https://doi.org/10.1111/j.2042-7158.2012.01497.x>
- Mendes, B. B., Connio, J., Avital, A., Yao, D., Jiang, X., Zhou, X., ... Conde, J. (2022). Nanodelivery of nucleic acids. *Nature Reviews Methods Primers*, 2, 24. <https://doi.org/10.1038/s43586-022-00104-y>
- Méndez-Ardoy, A., Díaz-Moscoso, A., Ortiz Mellet, C., Di Giorgio, C., Vierling, P., Benito, J. M., & García Fernández, J. M. (2015). Harmonized tuning of nucleic acid and lectin binding properties with multivalent cyclodextrins for macrophage-selective gene delivery. *RSC Advances*, 5(93), 76464–76471. <https://doi.org/10.1039/C5RA16087A>
- Mitchell, M. J., Billingsley, M. M., Haley, R. M., Wechsler, M. E., Peppas, N. A., & Langer, R. (2021). Engineering precision nanoparticles for drug delivery. *Nature Reviews Drug Discovery*, 20(2), 101–124. <https://doi.org/10.1038/s41573-020-0090-8>
- Mixich, L., Boomstra, E., Masuda, K., Li, S.-W., Nakashima, Y., Meng, F., ... Cabral, H. (2024). Ionizable polymeric micelles with phenylalanine moieties enhance intracellular delivery of self-replicating RNA for long-lasting protein expression in vivo. *Biomacromolecules*, 25(2), 1058–1067. <https://doi.org/10.1021/acs.biomac.3c01102>
- Moreno-Gutiérrez, D. S., del Toro-Ríos, X., Martínez-Sulvaran, N. J., Pérez-Altamirano, M. B., & Hernandez-Garcia, A. (2023). Programming the cellular uptake of protein-based viromimetic nanoparticles for enhanced delivery. *Biomacromolecules*, 24(4), 1563–1573. <https://doi.org/10.1021/acs.biomac.2c01295>
- Mousazadeh, H., Bonabi, E., & Zarghami, N. (2022). Stimulus-responsive drug/gene delivery system based on polyethylenimine cyclodextrin nanoparticles for potential cancer therapy. *Carbohydrate Polymer*, 276, Article 118747. <https://doi.org/10.1016/j.carbpol.2021.118747>
- Neva, T., Carbajo-Gordillo, A. I., Benito, J. M., Lana, H., Marcelo, G., Ortiz Mellet, C., ... García Fernández, J. M. (2020). Tuning the topological landscape of DNA-cyclodextrin nanocomplexes by molecular design. *Chemistry A European Journal*, 26(66), 15259–15269. <https://doi.org/10.1002/chem.202002951>
- Ooi, Y. J., Wen, Y., Zhu, J., Song, X., & Li, J. (2024). Codelivery of doxorubicin and p53 gene by β-cyclodextrin-based supramolecular nanoparticles formed via host–guest complexation and electrostatic interaction. *Biomacromolecules*, 25(5), 2980–2989. <https://doi.org/10.1021/acs.biomac.4c00123>
- Ortega-Caballero, F., Ortiz Mellet, C., Le Gourriérec, L., Guilloteau, N., Di Giorgio, C., Vierling, P., ... García Fernández, J. M. (2008). Tailoring β-cyclodextrin for DNA complexation and delivery by homogeneous functionalization at the secondary face. *Organic Letters*, 10(22), 5143–5146. <https://doi.org/10.1021/o10802081z>
- Ortega-Caballero, F., Santana-Armas, M. L., Tros de Ilarduya, C., Di Giorgio, C., Tripiet, R., Le Bris, N., ... Méndez-Ardoy, A. (2024). Trehalose-polyamine/DNA nanocomplexes: Impact of vector architecture on cell and organ transfection selectivity. *Journal of Materials Chemistry B*, 12(14), 3445–3452. <https://doi.org/10.1039/D3TB02889E>
- Ortiz Mellet, C., García Fernández, J. M., & Benito, J. M. (2011). Cyclodextrin-based gene delivery systems. *Chemical Society Reviews*, 40(3), 1586–1608. <https://doi.org/10.1039/C0CS00019A>
- Othman, M., Baker, A. T., Gupalo, E., Elsebaie, A., Bliss, C. M., Rondina, M. T., ... Parker, A. L. (2021). To clot or not to clot? Ad is the question—Insights on mechanisms related to vaccine-induced thrombotic thrombocytopenia. *Journal of Thrombosis and Haemostasis*, 19(11), 2845–2856. <https://doi.org/10.1111/jth.15485>
- Percec, V., & Sahoo, D. (2024). From Frank-Kasper quasicrystals, and biological membrane mimics to reprogramming in vivo the living factory to target the delivery of mRNA with one-component amphiphilic Janus dendrimers. *Biomacromolecules*, 25(3), 1353–1370. <https://doi.org/10.1021/acs.biomac.3c01390>
- Pezzoli, D., Giupponi, E., Mantovani, D., & Candiani, G. (2017). Size matters for in vitro gene delivery: Investigating the relationships among complexation protocol, transfection medium, size and sedimentation. *Scientific Reports*, 7, 44134. <https://doi.org/10.1038/srep44134>
- Philipp, J., Dabkowska, A., Reiser, A., Frank, K., Krzysztoń, R., Brummer, C., ... Rädler, J. O. (2023). pH-dependent structural transitions in cationic ionizable lipid mesophases are critical for lipid nanoparticle function. *Proceedings of the National Academy of Sciences of the United States of America*, 120(50), Article e2310491120. <https://doi.org/10.1073/pnas.2310491120>
- Press, W. H., Teukolski, S. A., Vetterling, W. T., & Flannery, B. P. (2007). *Numerical recipes: The art of scientific computing* (3rd ed.). Cambridge: Cambridge University Press.
- Ramezanpour, M., Schmidt, M. L., Bodnaruc, I., Kulkarni, J. A., Leung, S. S. W., Cullis, P. R., ... Tielemans, D. P. (2019). Ionizable amino lipid interactions with POPC: Implications for lipid nanoparticle function. *Nanoscale*, 11(30), 14141–14146. <https://doi.org/10.1039/C9NR02297J>
- Rana, R., Kant, R., Kumra, T., Gupta, S., Rana, D. S., & Ganguly, N. K. (2023). An update on SARS-CoV-2 immunization and future directions. *Frontiers in Pharmacology*, 14, 1125305. <https://doi.org/10.3389/fphar.2023.1125305>
- Rhan, H. P., Sun, J., Li, Z., Waymouth, R. M., Levy, R., & Wender, P. A. (2024). Isoprenoid CARTS_js: In vitro and in vivo mRNA delivery by charge-altering releasable transporters functionalized with Archaea-inspired branched lipids. *Biomacromolecules*. <https://doi.org/10.1021/acs.biomac.4c00373>. in press.
- Rivero-Barroja, G., Benito, J. M., Ortiz Mellet, C., & García Fernández, J. M. (2020). Cyclodextrin-based functional glyconanomaterials. *Nanomaterials*, 10(12), 2517. <https://doi.org/10.3390/nano10122517>
- Rueda-Fernández, M., Melguizo-Rodríguez, L., Costela-Ruiz, V. J., González-Acedo, A., Ramos-Torrecilla, J., & Illescas-Montes, R. (2022). The current status of COVID-19 vaccines. A scoping review. *Drug Discovery Today*, 27(11), Article 103336. <https://doi.org/10.1016/j.drudis.2022.08.004>
- Rutkauskaite, A., White, L. J., Hilton, K. L. F., Picci, G., Croucher, L., Caltagirone, C., & Hiscock, J. R. (2022). Supramolecular self-associating amphiphiles: Determination of molecular self-association properties and calculation of critical micelle concentration using a high-throughput, optical density based methodology. *Organic & Biomolecular Chemistry*, 20(30), 5999–6006. <https://doi.org/10.1039/D2OB00066K>
- Sansone, F., Dudic, M., Donofrio, G., Rivetti, C., Baldini, L., Casnati, A., ... Ungaro, R. (2006). DNA condensation and cell transfection properties of guanidinium calixarenes: Dependence on macrocycle lipophilicity, size, and conformation. *Journal of the American Chemical Society*, 128(45), 14528–14536. <https://doi.org/10.1021/ja0634425>
- Schoenmaker, L., Witzigmann, D., Kulkarni, J. A., Verbeke, R., Kersten, G., Jiskoot, W., & Crommelin, D. J. A. (2021). mRNA-lipid nanoparticle COVID-19 vaccines: Structure and stability. *International Journal of Pharmaceutics*, 601, Article 120586. <https://doi.org/10.1016/j.ijpharm.2021.120586>
- Sehgal, V., Pandey, S. P., & Singh, P. K. (2024). Prospects of charged cyclodextrins in biomedical applications. *Carbohydrate Polymers*, 323, Article 121348. <https://doi.org/10.1016/j.carbpol.2023.121348>
- Singh, N., Maretz, C., Boudon, J., Millot, N., Saviot, L., & Maurizi, L. (2021). In vivo protein corona on nanoparticles: Does the control of all material parameters orient the biological behavior? *Nanoscale Advances*, 3(5), 1209–1229. <https://doi.org/10.1039/dna00863j>
- Sinha, A. K., & Equbal, D. (2019). Thiol-ene reaction: Synthetic aspects and mechanistic studies of an anti-Markovnikov-selective hydrothiolation of olefins. *Asian Journal of Organic Chemistry*, 8(1), 32–47. <https://doi.org/10.1002/ajoc.201800639>
- Smith, S. A., Selby, L. I., Johnston, A. P. R., & Such, G. K. (2019). The endosomal escape of nanoparticles: Toward more efficient cellular delivery. *Bioconjugate Chemistry*, 30(2), 263–272. <https://doi.org/10.1021/acs.bioconjchem.8b00732>
- Sun, Y., Cronin, M. F., Mendonça, M. C. P., Guo, J., & O'Driscoll, C. M. (2023). Sialic acid-targeted cyclodextrin-based nanoparticles deliver CSF-1R siRNA and reprogram tumour-associated macrophages for immunotherapy of prostate cancer. *European Journal of Pharmaceutical Sciences*, 185, Article 106427. <https://doi.org/10.1016/j.ejps.2023.106427>
- Sung, Y. K., & Kim, S. W. (2019). Recent advances in the development of gene delivery systems. *Biomaterials Research*, 23, 8. <https://doi.org/10.1186/s40824-019-0156-z>
- Symens, N., Méndez-Ardoy, A., Díaz-Moscoso, A., Sánchez-Fernández, E., Remaut, K., Demeester, J., ... Rejman, J. (2012). Efficient transfection of hepatocytes mediated

- by mRNA complexed to galactosylated cyclodextrins. *Bioconjugate Chemistry*, 23(6), 1276–1289. <https://doi.org/10.1021/bc3001003>
- Taharabaru, T., Kihara, T., Obata, A., Onodera, Wen, R. Y., Li, J., ... Higashi, T. (2024). Cyclodextrin-based tailored polyrotaxanes for highly efficient delivery of the genome-editing molecule. *Carbohydrate Polymers*, 323, Article 121443. <https://doi.org/10.1016/j.carbpol.2023.121443>
- Udachin, K. A., & Ripmeester, J. A. (1998). A novel mode of inclusion for pyrene in β -cyclodextrin compounds: The crystal structures of β -cyclodextrin with cyclohexanol and pyrene, and with n-octanol and pyrene. *Journal of the American Chemical Society*, 120(5), 1080–1081. <https://doi.org/10.1021/ja972156d>
- van Straten, D., Sork, H., van de Schepop, L., Frunt, R., Ezzat, K., & Schiffelers, R. M. (2024). Biofluid specific protein coronas affect lipid nanoparticle behavior in vitro. *Journal of Controlled Release*, 373, 481–492. <https://doi.org/10.1016/j.jconrel.2024.07.044>
- Verbeke, R., Lentacker, I., De Smedt, S. C., & Dewitte, H. (2021). The dawn of mRNA vaccines: The COVID-19 case. *Journal of Controlled Release*, 333, 511–520. <https://doi.org/10.1016/j.jconrel.2021.03.043>
- Villari, V., Mazzaglia, A., Darcy, R., O'Driscoll, C. M., & Micali, N. (2013). Nanostructures of cationic amphiphilic cyclodextrin complexes with DNA. *Biomacromolecules*, 14(3), 811–817. <https://doi.org/10.1021/bm3018609>
- Wang, J., Xie, L., Wang, T., Wu, F., Meng, J., Liu, J., & Xu, H. (2017). Visible light-switched cytosol release of siRNA by amphiphilic fullerene derivative to enhance RNAi efficacy in vitro and in vivo. *Acta Biomaterialia*, 59, 158–169. <https://doi.org/10.1016/j.actbio.2017.05.031>
- Wang, J., Zaidi, S. S. A., Hasnain, A., Guo, J., Ren, X., Xia, S., ... Feng, Y. (2018). Multitargeting peptide-functionalized star-shaped copolymers with comblike structure and a POSS-Core to effectively transfect endothelial cells. *ACS Biomaterials Science & Engineering*, 4(6), 2155–2168. <https://doi.org/10.1021/acsbiomaterials.8b00235>
- Wang, Z., Li, X., Feng, F., Hong, C., Sun, Z., Tian, W., Yu, K., & Liu, H. (2023). Dynamic co-assembly behaviors of polyoxometalates and giant surfactants in dual solvents. *Giant*, 13, Article 100142. <https://doi.org/10.1016/j.giant.2023.100142>
- Whitfield, C. J., Zhang, M., Winterwerber, P., Wu, Y., Ng, D. Y. W., & Weil, T. (2021). Functional DNA-polymer conjugates. *Chemical Reviews*, 121(18), 11030–11084. <https://doi.org/10.1021/acs.chemrev.0c01074>
- Xiao, T., Qi, L., Zhong, W., Lin, C., Wang, R., & Wang, L. (2019). Stimuli-responsive nanocarriers constructed from pillar[n]arene-based supra-amphiphiles. *Materials Chemistry Frontiers*, 3(10), 1973–1993. <https://doi.org/10.1039/C9QM00428A>
- Xu, L., & Zhang, W.-B. (2018). The pursuit of precision in macromolecular science: Concepts, trends, and perspectives. *Polymer*, 155, 235–247. <https://doi.org/10.1016/j.polymer.2018.09.017>
- Yin, G.-Z., Zhang, W.-B., & Cheng, S. Z. D. (2017). Giant molecules: Where chemistry, physics, and bio-science meet. *SCIENCE CHINA Chemistry*, 60(3), 338–352. <https://doi.org/10.1007/s11426-016-0436-x>
- Yuan, W., Ma, J., Zhao, Z., & Liu, S. (2020). Self-assembly of supramolecular DNA amphiphiles through host-guest interaction and their stimuli-responsiveness. *Macromolecular Rapid Communications*, 41(9), Article 2000022. <https://doi.org/10.1002/marc.202000022>
- Zhang, D., Atochina-Vasserman, E. N., Lu, J., Maurya, D. S., Xiao, Q., Liu, M., ... Percec, V. (2022). The unexpected importance of the primary structure of the hydrophobic part of one-component ionizable amphiphilic Janus dendrimers in targeted mRNA delivery activity. *Journal of the American Chemical Society*, 144(11), 4746–4753. <https://doi.org/10.1021/jacs.2c00273>
- Zhang, D., Atochina-Vasserman, E. N., Maurya, D. S., Huang, N., Xiao, Q., Ona, N., ... Percec, V. (2021). One-component multifunctional sequence-defined ionizable amphiphilic Janus dendrimer delivery systems for mRNA. *Journal of the American Chemical Society*, 143(31), 12315–12327. <https://doi.org/10.1021/jacs.1c05813>
- Zhang, D., Atochina-Vasserman, E. N., Maurya, D. S., Liu, M., Xiao, Q., Lu, J., ... Percec, V. (2021). Targeted delivery of mRNA with one-component ionizable amphiphilic Janus dendrimers. *Journal of the American Chemical Society*, 143(43), 17975–17982. <https://doi.org/10.1021/jacs.1c09585>
- Zu, H., & Gao, D. (2021). Non-viral vectors in gene therapy: Recent development, challenges, and prospects. *AAPS Journal*, 23(4), 78. <https://doi.org/10.1208/s12248-021-00608-7>
- Zyryanov, G. V., Kopchuk, D. S., Kovalev, I. S., Santra, S., Majee, A., & Ranu, B. C. (2023). Pillararenes as promising carriers for drug delivery. *International Journal of Molecular Sciences*, 24(6), 5167. <https://doi.org/10.3390/ijms24065167>